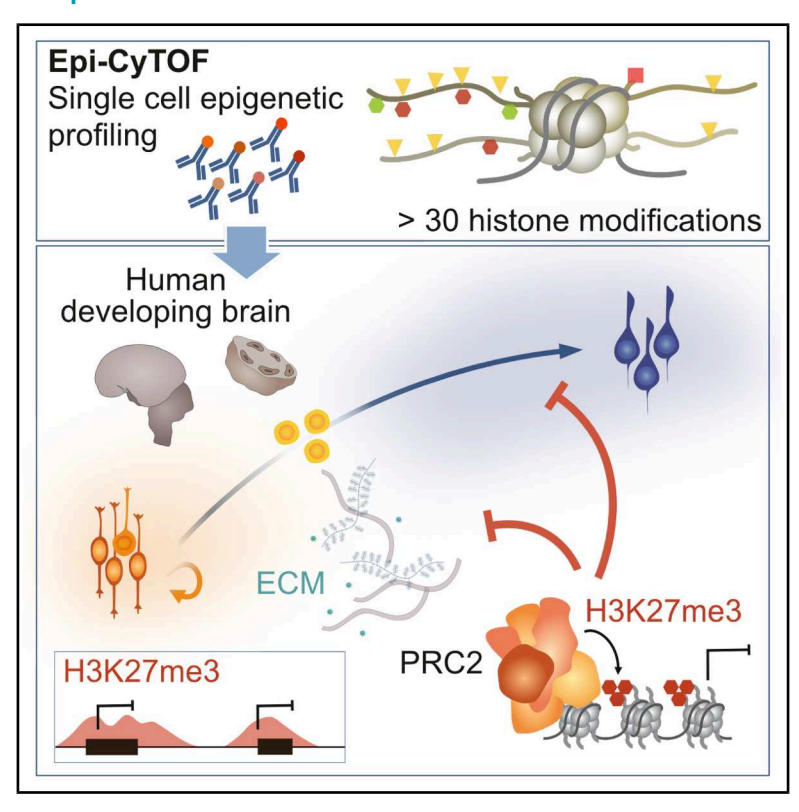
Neuron

Epigenome profiling identifies H3K27me3 regulation of extracellular matrix composition in human corticogenesis

Graphical abstract



Authors

Nora Ditzer, Ezgi Senoglu, Annika Kolodziejczyk, ..., Franziska Baenke, Claudia Peitzsch, Mareike Albert

Correspondence

mareike.albert@tu-dresden.de

In brief

Ditzer, Senoglu, et al. report that epigenetic factors of the Polycomb group regulate not only neurogenic gene expression programs but also the composition of the extracellular matrix in the human developing neocortex. Inhibition of Polycomb repressive complex 2 promotes neural progenitor cell differentiation, resulting in smaller brain organoids.

Highlights

- Epi-CyTOF enables simultaneous single-cell analysis of more than 30 epigenetic marks
- H3K27me3 shows strong cell-type-specific enrichment in the human developing neocortex
- Inhibition of PRC2 promotes neural progenitor cell differentiation
- PRC2 regulates extracellular matrix composition in human cortical organoids





Neuron



Article

Epigenome profiling identifies H3K27me3 regulation of extracellular matrix composition in human corticogenesis

Nora Ditzer,^{1,10} Ezgi Senoglu,^{1,10} Annika Kolodziejczyk,¹ Theresa M. Schütze,¹ Aikaterina Nikolaidi,¹ Karolin Küster,¹ Katrin Sameith,² Sevina Dietz,¹ Razvan P. Derihaci,^{3,4} Cahit Birdir,^{3,5} Anne Eugster,¹ Mike O. Karl,^{1,6} Andreas Dahl,² Pauline Wimberger,^{3,4} Franziska Baenke,^{7,8,9} Claudia Peitzsch,¹ and Mareike Albert^{1,11,*}

¹Center for Regenerative Therapies TU Dresden, TUD Dresden University of Technology, 01307 Dresden, Germany

²DRESDEN-concept Genome Center, c/o CMCB Center for Molecular and Cellular Bioengineering, Technology Platform of the TUD Dresden University of Technology, 01062 Dresden, Germany

³Department of Gynaecology and Obstetrics, Technische Universität Dresden, 01307 Dresden, Germany

⁴National Center for Tumor Diseases, 01307 Dresden, Germany

⁵Center for Feto/neonatal Health, Technische Universität Dresden, 01307 Dresden, Germany

⁶German Center for Neurodegenerative Diseases, 01307 Dresden, Germany

⁷Department of Visceral, Thoracic and Vascular Surgery, Medical Faculty and University Hospital Carl Gustav Carus, Technische Universität Dresden, 01307 Dresden, Germany

⁸National Center for Tumor Diseases, Dresden, 01307 Dresden, Germany

⁹German Cancer Consortium, 01307 Dresden, Germany

¹⁰These authors contributed equally

¹¹Lead contact

*Correspondence: mareike.albert@tu-dresden.de https://doi.org/10.1016/j.neuron.2025.06.016

SUMMARY

Epigenetic mechanisms regulate gene expression programs during neurogenesis, but the extent of epigenetic remodeling during human cortical development remains unknown. Here, we characterize the epigenetic landscape of the human developing neocortex by leveraging Epi-CyTOF, a mass-cytometry-based approach for the simultaneous single-cell analysis of more than 30 epigenetic marks. We identify Polycomb repressive complex 2 (PRC2)-mediated H3K27me3 as the modification with the strongest cell-type-specific enrichment. Inhibition of PRC2 in human cortical organoids resulted in a shift of neural progenitor cell (NPC) proliferation toward differentiation. Cell-type-specific profiling of H3K27me3 identified neuronal differentiation and extracellular matrix (ECM) genes in the human neocortex. PRC2 inhibition resulted in increased production of the ECM proteins Syndecan 1 and laminin alpha 1. Overall, this study comprehensively characterizes the epigenetic state of specific neural cell types and highlights a novel role for H3K27me3 in regulating the ECM composition in the human developing neocortex.

INTRODUCTION

The neocortex, responsible for higher cognitive abilities in humans, develops from a pool of neural progenitor cells (NPCs) that give rise to diverse cell types. Cortical development involves a tight balance of NPC self-renewal and differentiation, ensuring appropriate cellular output and brain size.^{1–4}

The proliferative capacity of distinct NPC types differs greatly. Radial glia (RG) have the ability to self-renew, thereby replenishing the progenitor pool, and to give rise to intermediate progenitor cells (IPs) that are more neurogenic.^{5–7} Underlying these cell fate transitions are precise temporal and spatial gene expression patterns that are tightly controlled by epigenetic regulation,^{8–11} including posttranslational histone modifi-

cations that occur in a huge diversity and fulfill important functions. 12,13

Proteins of the Trithorax and Polycomb systems were shown to play major roles in NPC differentiation. 14,15 These groups of epigenetic writers constitute an evolutionarily conserved system, displaying antagonistic functions to maintain active and repressed chromatin states. 16,17 Polycomb group proteins have been implicated in the regulation of developmental timing and transcriptional programs in the mouse developing cortex. 18-21

Less is known about the regulation of human neocortex development, yet, many epigenetic factors have been linked to developmental disorders associated with brain phenotypes and intellectual disability.^{22,23} Only recently, the first studies in





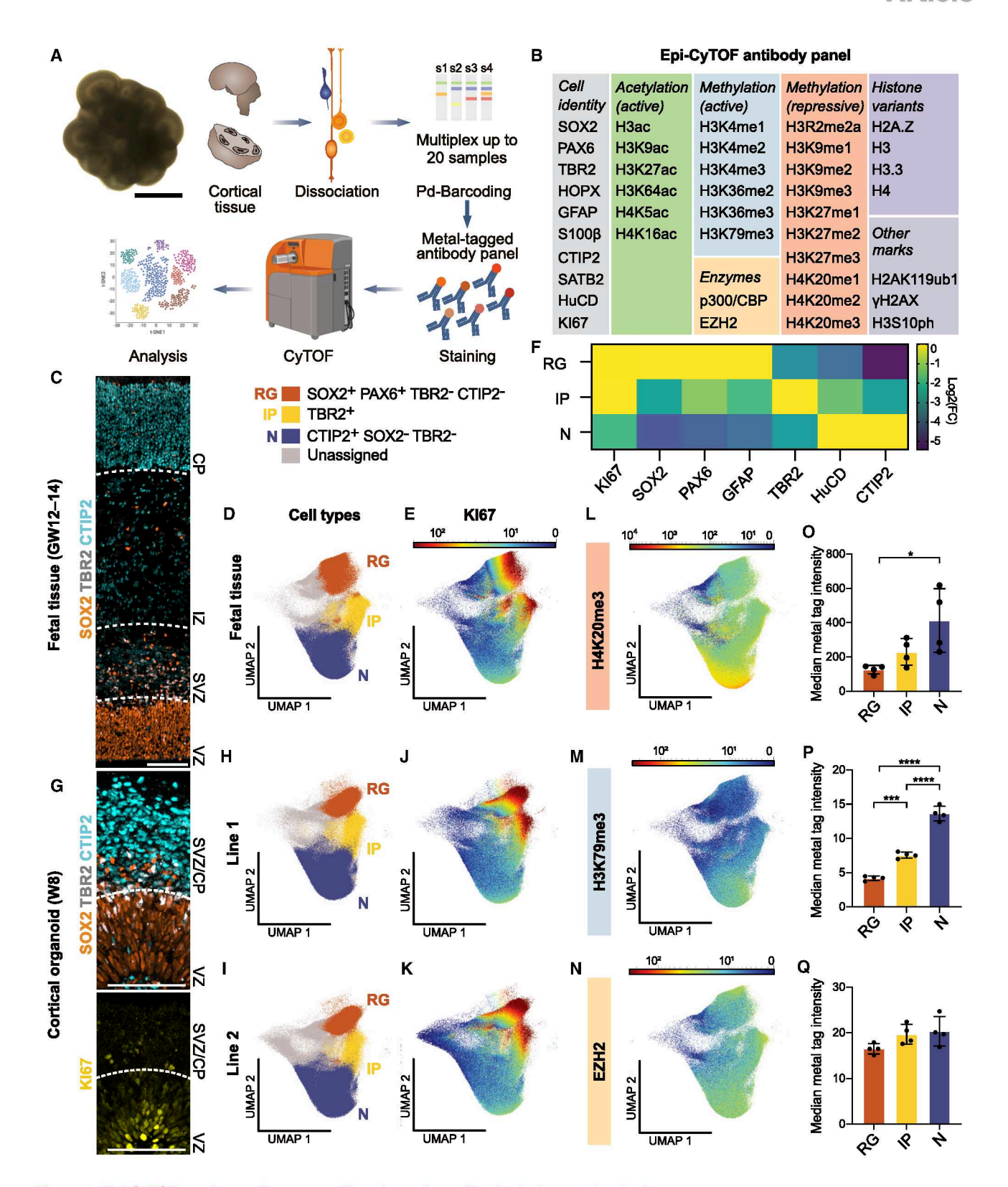


Figure 1. Epi-CyTOF resolves cell-type-specific epigenetic profiles in the human developing neocortex

(A) Experimental workflow of Epi-CyTOF.

(B) Epi-CyTOF antibody panel.

(C) Immunofluorescence staining for SOX2, TBR2, and CTIP2 of human fetal tissue (GW12–GW14).



advanced human models were performed. Polycomb-mediated regulation was shown to control the exit from pluripotency in early human brain organoids.²⁴ Moreover, in concert with two other epigenetic modifiers, Polycomb proteins were shown to contribute to an epigenetic barrier in NPCs that mediates the protracted maturation of human neurons.²⁵

Currently, we lack a clear understanding of the complexity of epigenetic remodeling during human cortical neurogenesis. Such knowledge may enable future research on diagnostic and therapeutic approaches for human disorders involving epigenetic changes. Powerful single-cell technologies are available for the analysis of gene expression, open chromatin, DNA methylation, and 3D chromatin structure, even in combination, whereas single-cell analysis of histone modifications is just emerging but typically limited to few modifications. ^{24,27,28}

Here, we apply an innovative, highly multiplexed approach, Epi-CyTOF, ^{29,30} to study a large number of epigenetic modifications at single-cell level in the human developing neocortex. We then focus on H3K27me3, the modification that displays the most substantial differences between neural cell types. Based on pharmacological inhibition of Polycomb repressive complex 2 (PRC2) and cell-type-specific profiling of H3K27me3 across the genome, we propose a mechanism by which Polycomb group proteins regulate cell fate in human cortical development.

RESULTS

Epi-CyTOF resolves epigenetic marks at single-cell resolution in the human developing neocortex

Epigenetic regulation of gene expression involves different layers, including a large number of histone modifications. To identify the histone marks that display global changes across neural cell types of the human developing neocortex, and that may therefore be important for neural cell fate, we adopted a cytometry by timeof-flight-based method for epigenetic analysis, termed Epi-CvTOF^{29,30} (Figure 1A). We have designed a custom panel of metal isotope-conjugated antibodies targeting 10 cell-type markers, to resolve the cellular heterogeneity of the developing neocortex, and 31 histone modifications and epigenetic enzymes (Figure 1B; Table S1). The specificity of most antibodies was previously validated by pharmacological inhibition and knockdown or overexpression of the responsible epigenetic modifiers^{29,30} (Table S1). The antibody panel was used to stain cell suspensions of human fetal tissue (gestation week [GW] 12-14) and human cortical organoids³¹ from two independent induced pluripotent stem cell (iPSC) lines (week [W] 8). Each tissue type included four replicates, all of which were combined by palladium-based barcoding to reduce batch effects. Clustering of viable cell populations from human fetal tissue, based on the cell-type markers SOX2, PAX6, TBR2, and CTIP2, separated three main cell populations, specifically RG, IPs, and neurons (Figures 1C and 1D), which were highly consistent across replicates (Figures S1A–S1C). The cell populations were further validated by expression of Kl67 in RG and IP, expression of GFAP in RG, and expression of HuCD in neurons (Figures 1E and 1F). Human brain organoids have become an essential tool for functional studies of human neurogenesis. ^{22,32,33} To assess whether epigenetic marks across our broad panel were conserved in these *in vitro* models, we performed Epi-CyTOF analysis on human cortical organoids (Figure 1G). This revealed that cell-type clustering and staining of cell-type markers (Figures 1H–1K and S1A–S1C) were highly similar to human fetal tissue.

Next, we analyzed Epi-CyTOF data of histone modifications in human fetal tissue and cortical organoids, providing single-cell epigenetic information as exemplified for H4K20me3, H3K79me3, and EZH2 (Figures 1L–1Q and S1D). We then determined the mean metal tag intensities for all 31 epigenetic readouts for RG, IPs, and neurons for each individual replicate (Figures S2A–S2C; Table S2), highlighting the power of the methodology to determine changes in global levels of a large number of epigenetic modifications across 12 samples at once. This revealed that many modifications display differential enrichment across different neural cell types.

Taken together, Epi-CyTOF not only is able to resolve the cellular heterogeneity of the human developing neocortex but also provides single-cell epigenetic information for a large number of posttranslational histone modifications.

H3K27me3 is highly enriched in cortical neurons compared with NPCs

To identify the histone modifications that most strongly change from RG to neurons, we plotted the fold change of metal tag intensities for all epigenetic markers analyzed by Epi-CyTOF (Figures 2A and S2D–S2H). In human fetal tissue, 13 of the 31 markers had a significantly higher staining intensity in neurons compared with RG, including both active and repressive histone modifications (Figures 10–1Q, 2C, 2D, and S3). Except for active H3K4me2/3, the remaining modifications did not show significant cell-type-specific enrichment (Figure S3). The enrichment of many histone modifications in neurons is in line with the view that epigenetic marks accumulate with the progression of cell fate commitment during lineage specification, ³⁴ and our data suggest that this involves both active and repressive histone modifications in the human developing neocortex.

The histone modification that showed one of the strongest changes from RG to neurons in human fetal tissue was

⁽D and E) UMAP analysis of cell-type clustering (D) and color-continuous scatter plots of the cell proliferation marker Kl67 (E) for human fetal tissue. Scale represents metal isotope tag intensity.

⁽F) Heatmap of log2 fold changes (FCs) of median metal tag intensities for cell-type markers in fetal tissue (4 tissue samples from 2 individuals).

⁽G) Immunofluorescence for SOX2, TBR2, and CTIP2 (top) and KI67 (bottom) of cortical organoids (W8).

⁽H–K) UMAP of cell-type clusters (H and I) and Kl67 intensity (J and K) for cortical organoids (W8) generated from iPSC lines 1 and 2 (4 replicates per cell line from independent organoid batches).

⁽L-N) UMAP color-continuous scatter plots in human fetal tissue.

⁽O-Q) Median metal tag intensities of markers in (L)-(N).

Scale bars, (A) 1 mm, (C and G) 100 μ m. Bar graphs represent mean values. Error bars represent SD of 4 tissue samples from 2 individuals. One-way ANOVA with Tukey's post hoc test; ****p < 0.0001, ***p < 0.001, and *p < 0.005. N, neuron.



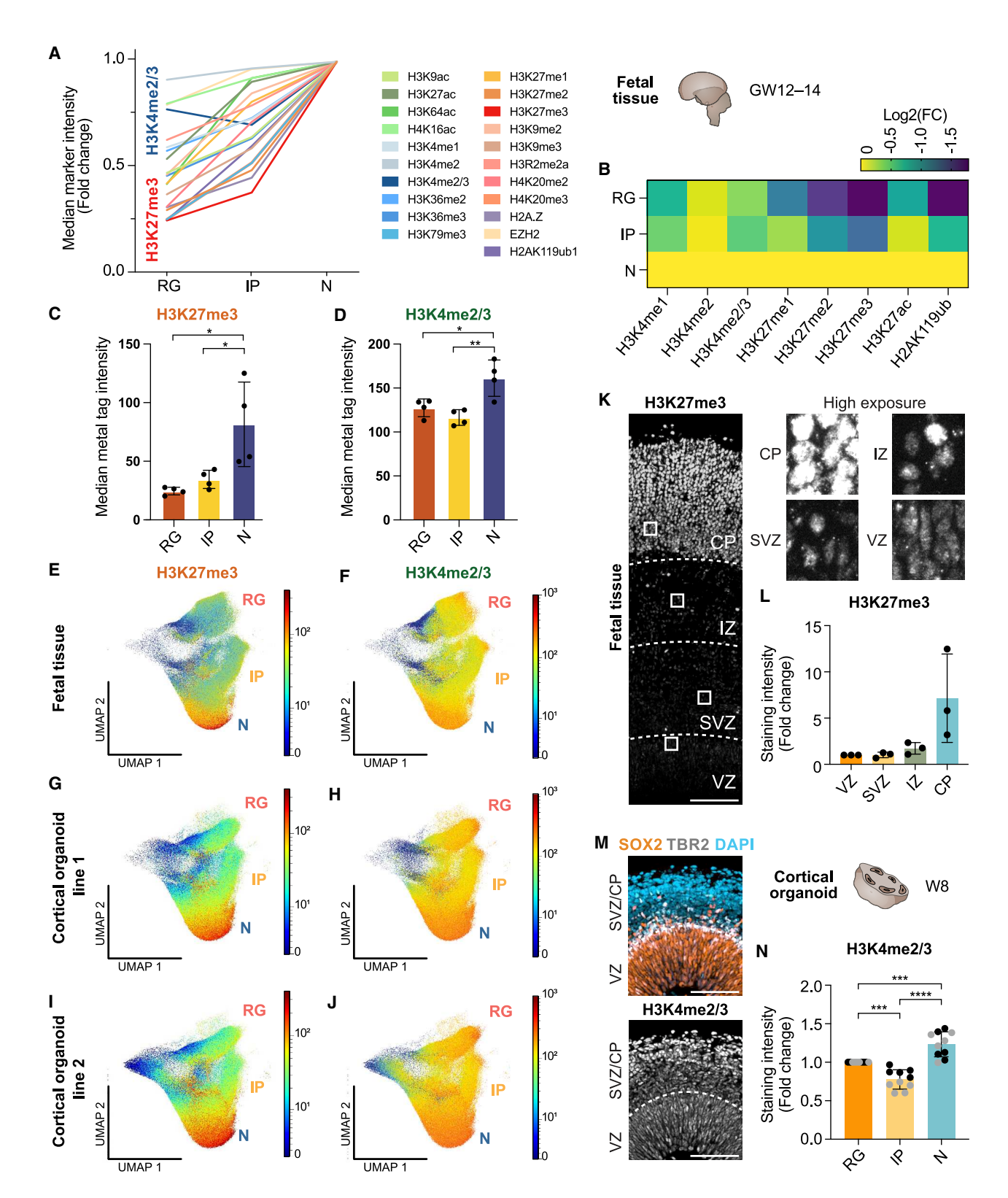


Figure 2. Epi-CyTOF reveals a strong enrichment of H3K27me3 in human cortical neurons compared with NPCs

(A) Line plot displaying epigenetic marks with increasing abundance from RG to N. Values represent fold change of Epi-CyTOF median metal tag intensities in human fetal tissue.

(B) Heatmap of Log2 fold changes of median metal tag intensities for epigenetic marks.

(legend continued on next page)



H3K27me3 (Figures 2A-2C). This modification also exhibited a strong change from RG to neurons in cortical organoids from both iPSC lines (Figures S2D and S2E). H3K27me3 is a repressive modification mediated by PRC2 and counteracted by active H3K4me3. 16,17 Additional Polycomb-associated modifications, specifically H3K27me2 and H2AK119ub1, also displayed differential enrichment in neurons compared with RG (Figures 2A, 2B, and S3). In contrast, H3K4me2/3 was detected in all cell types, with a slight decrease from RG to IPs, accompanied by a minor increase in neurons (Figure 2D). The patterns of H3K27me3 and H3K4me2/3 staining intensity across the three major cell-type clusters were highly similar in human fetal tissue and cortical organoids (Figures 2E-2J).

To independently verify these findings, we performed immunohistochemistry for H3K27me3 on human fetal tissue, using a different primary antibody (Figure 2K). Quantification of the staining intensity confirmed the lower levels of H3K27me3 in the ventricular (VZ) and subventricular (SVZ) zone, containing RG and IPs, respectively, and the strong enrichment of H3K27me3 in the cortical plate (CP), where neurons reside (Figure 2L). Likewise, immunohistochemistry for H3K4me2/3 of human tissue and cortical organoids confirmed the Epi-CyTOF staining pattern, with slightly lower levels in IPs compared with RG and neurons (Figures 2M, 2N, S4A, and S4B), indicating that Epi-CyTOF is able to detect small differences in histone modifications between cell types. Overall, these findings suggest that analysis of histone modifications by Epi-CyTOF was highly robust across multiple replicates in complex tissue samples.

To further investigate the differential enrichment pattern of H3K27me3 in the human developing neocortex, we asked whether PRC2 components were also differentially expressed. Both gene expression analysis of published transcriptome datasets³⁵ and immunohistochemistry for EZH2 and SUZ12 indicated that PRC2 core components were uniformly expressed across the cortical wall of the human fetal neocortex (Figures S4C-S4E), in line with Epi-CyTOF data (Figures 1N and 1Q). A time course of human cortical organoid development showed that PRC2 expression is largely uniform from W2 to W10 (Figures S4F and S4G). Interestingly, however, while H3K27me3 is initially homogenously distributed in human cortical organoids (W2-W4), H3K27me3 is strongly enriched in neurons compared with progenitors from W6 onward, mirroring the pattern in human fetal tissue (Figures 2K and 2L), despite uniform distribution of PRC2 (Figures S4C-S4H). The mechanism underlying neuronspecific enrichment of H3K27me3 remains to be resolved. Of the accessory subunits, only PHF19, whose deletion was shown to result in increased H3K27me3 in prostate cancer, 36 showed a relevant expression pattern with higher levels in RG compared with neurons. Alternatively, the differential cellular metabolism of NPCs and neurons may affect the availability of metabolites for epigenetic reactions, contributing to global differences in histone modification during cortical development.³⁷

In summary, Epi-CyTOF identified PRC2-mediated H3K27me3 as the most differentially distributed histone modification between RG and neurons.

Genome-wide H3K27me3 profiles distinguish neural cell populations

We next aimed to elucidate the distribution of H3K27me3 and H3K4me2/3 throughout the genome. Therefore, we isolated nuclei from human fetal tissue (GW12-GW14), sorted major cell populations using fluorescence-activated nuclei sorting (FANS), and performed cleavage under targets and tagmentation (CUT&Tag)³⁸ (Figure 3A). RG, IPs, and neurons were isolated based on expression of the cell-type markers PAX6, TBR2, and CTIP2, respectively (Figures S5A and S5B). Cell identity of the sorted populations was validated by expression of additional marker genes (Figure S5C). To prevent potential unspecific signal from the sorting antibodies in CUT&Tag, we applied a blocking step using Fab fragments.³⁹ Successful blocking was confirmed by the lack of regions significantly enriched for H3K27me3 in an unstained versus stained cell population (Figure S5D).

Applying this cell-type-specific CUT&Tag strategy, we found a small set of regions strongly enriched for H3K27me3 in RG and IPs, whereas H3K27me3 was enriched at low levels at additional regions in neurons (Figure 3B). In contrast, the distribution pattern of H3K4me2/3 was more similar between cell types (Figure 3C). This was also reflected in the principal-component analysis (PCA), in which H3K27me3 of RG and IPs was clearly separated from the neurons, whereas all three cell types clustered together for H3K4me2/3 (Figure 3D). Z scores of the top 20,000 regions for H3K27me3 and H3K4me2/3 further confirmed this observation (Figure 3E).

To identify differentially enriched regions for H3K27me3 and H3K4me2/3 in individual cell types, we used DESeq2 (p adjust \leq 0.05; log2FC \geq 1). Since we did not detect any regions specifically enriched for H3K27me3 in IPs, we pooled RG and IPs, referred to as "NPCs." In total, 3,918 neuron- and 2,301 NPCspecific regions were detected for H3K27me3 (Figure 3F; Table S3). Compared with the NPC-specific regions, neuronspecific regions displayed, on average, lower enrichment of H3K27me3. In contrast, only 36 neuron- and 267 NPC-specific regions were detected for H3K4me2/3 (Figure 3G), despite the overall higher number of binding sites marked by H3K4me2/3 compared with H3K27me3 (Figures S5E and S5F). Cell-typespecific distribution of H3K27me3 was, for example, found at the transcription factor genes HES1 and TBR1 (Figures 3H-3K).

⁽C and D) Median metal tag intensities for H3K27me3 (C) and H3K4me2/3 (D) in human fetal tissue.

⁽E-J) Uniform manifold approximation and projection (UMAP) color-continuous scatter plots.

⁽K) Immunofluorescence of H3K27me3 of human fetal tissue (GW12-GW14), including higher exposure insets of each zone (right).

⁽L) Quantification of H3K27me3 intensity in human fetal tissue (relative to the VZ).

⁽M) Immunofluorescence for SOX2, TBR2, and CTIP2 (top) and H3K4me2/3 (bottom) of cortical organoids from iPSC line 1.

⁽N) Quantification of H3K4me2/3 (relative to RG).

Scale bars, 100 µm. Bar graphs represent mean values. Error bars represent SD; (C) and (D), of 4 replicates; (L), of 3 tissue samples from independent individuals; (N), of 10 organoids from 2 batches. (C), (D), (L), (N), one-way ANOVA with Tukey's post hoc test; ****p < 0.001, ***p < 0.001, ***p < 0.01, and *p < 0.05. N, neuron.



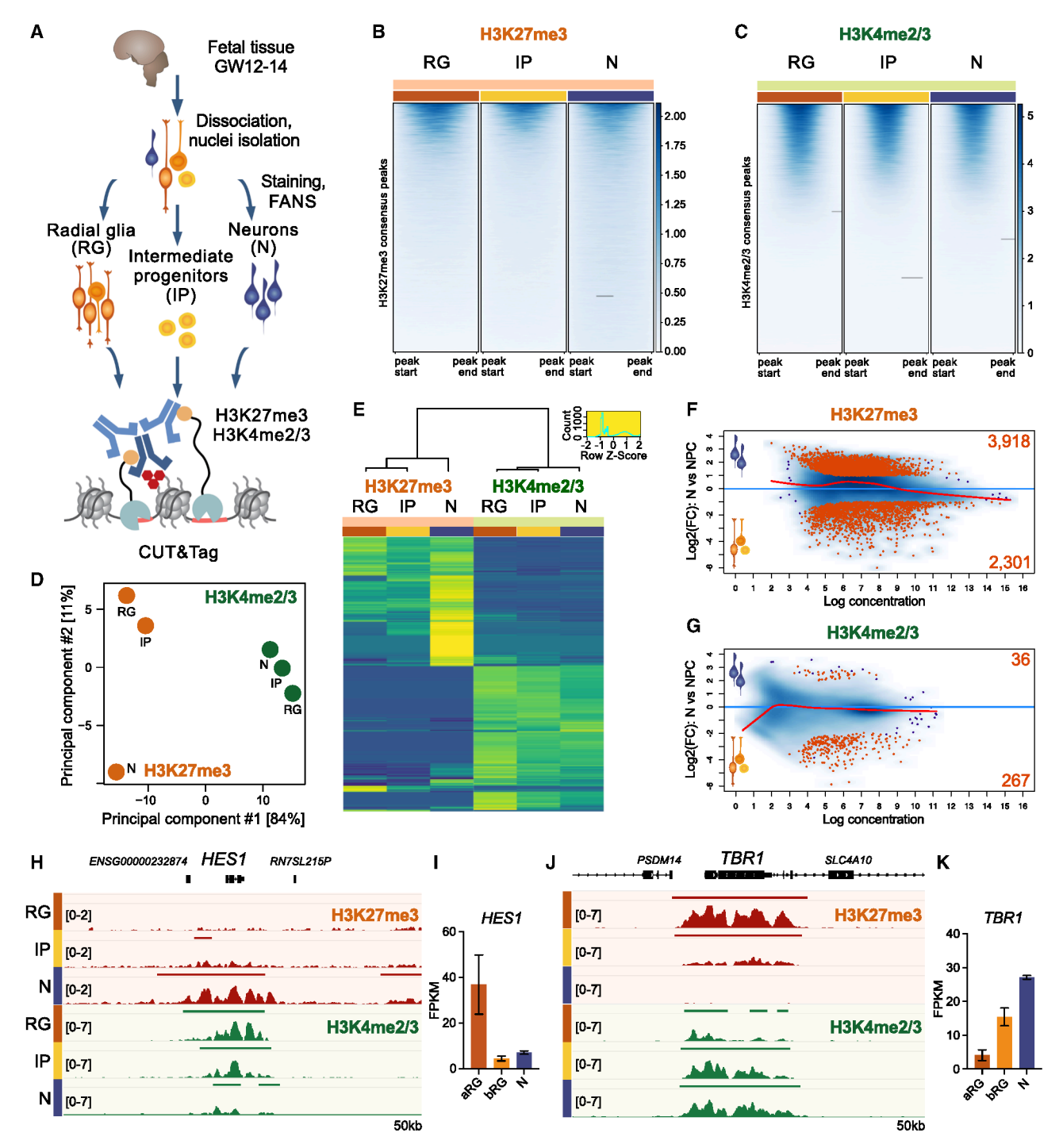


Figure 3. H3K27me3 profiles distinguish NPCs and neurons in the human developing neocortex

- (A) Experimental scheme for cell-type-specific CUT&Tag from human fetal tissue (two tissue samples from independent individuals).
- (B and C) Heatmaps of the enrichment of H3K27me3 (B) and H3K4me2/3 (C) in a set of consensus peaks (mean of 2 samples).
- (D) PCA analysis (each dot represents the average of 2 samples).
- (E) Heatmaps for H3K27me3 and H3K4me2/3 peaks. Plotted are Z scores for the top 20K regions, sorted by standard deviation.
- (F and G) MA plot illustrating differential enrichment of H3K27me3 (F) and H3K4me2/3 (G) between neurons and NPCs (combining RG and IP). Regions significantly enriched in one cell population are marked in red (p adjust. < 0.05; logFC > 1).
- (H) Tracks of H3K27me3 and H3K4me2/3 at the HES1 genomic locus.
- (I) Corresponding HES1 mRNA levels in human fetal cortex (data from Florio et al. 35).
- (J) Tracks of H3K27me3 and H3K4me2/3 at the neuronal gene locus TBR1.
- (K) TBR1 mRNA levels.



Overall, these results are in line with the global levels of H3K27me3 and H3K4me2/3 characterized by Epi-CyTOF. Using cell-type-specific epigenomics, we found the repressive H3K27me3 mark to become progressively enriched throughout the neuronal differentiation trajectory, while we did not observe comparable changes for the active H3K4me2/3 mark.

Inhibition of PRC2 induces a shift in NPC proliferation toward differentiation in human cortical organoids

Both, the global enrichment of H3K27me3 in neurons and the cell-type-specific genome-wide distribution of H3K27me3, suggest a role of PRC2 in regulating cell fate transitions in the human developing neocortex. Prior to this study, the role of PRC2 in regulating neuronal maturation has been described in detail.⁴⁰ Thus, we focused on functionally investigating the role of PRC2 in NPCs throughout human corticogenesis. We applied pharmacological inhibition of EED, 41 a core subunit of PRC2, to cortical organoids from W3 to W8 of culture (Figure 4A), using 5 μM EED226 (EEDi). This concentration resulted in an almost complete depletion of H3K27me3 after 5 weeks of treatment, without compromising organoid structure (Figures 4B, 4C, and S6A), whereas a higher inhibitor concentration of 10 µM induced cell death in test experiments after 1 week of organoid culture (Figure S6B). Of note, H3K27me3 was also abolished in neurons (Figure 4B), which have a very high enrichment of this modification and represent post-mitotic cells, which do not dilute histone methylation during DNA replication.

To assess the effects of H3K27me3 depletion on cortical organoid development, we first analyzed the mitotic marker phospho-histone 3 (PH3). We found a significant decrease in ventricular and total mitosis compared with the DMSO control (Figures 4D and 4E). Moreover, examination of the cell proliferation marker KI67 revealed a reduction in the percentage of KI67positive cells out of total cells and in the SVZ/CP (Figures S6C and S6D), where IPs reside. This was mirrored by an increase in the percentage of PAX6/TBR2 double-positive cells among KI67-positive cells in the VZ, at the cost of PAX6 single-positive cells (Figures S6C and S6E). Loss of H3K27me3 also resulted in a significant reduction of SOX2 single-positive RG in the VZ (Figures 4F and 4G). Moreover, consistent with previous results of EZH2 inhibition in human forebrain organoids, 25 we observed a significant increase in CTIP2-positive neurons after 5 weeks of treating cortical organoids with EEDi. These differences in celltype proportions were not yet observable after 2 weeks of EEDi treatment (Figures S6F and S6G), suggesting that PRC2 inhibition and subsequent loss of H3K27me3 require longer time spans to manifest in cellular phenotypes.

So far, our observations suggest that loss of H3K27me3 induces a shift of NPC proliferation toward differentiation in human cortical organoids. Such a shift would eventually be expected to result in lower neuronal output due to a reduction of the NPC pool. Indeed, total organoid size was significantly reduced by EEDi treatment (Figures 4H and 4I), accompanied by a decrease in the VZ thickness in ventricle-like regions (Figures S6H and S6I). Staining for cleaved caspase-3 (CC3) confirmed that this change in size was not caused by increased apoptosis in the inhibitor-treated organoids (Figures S6J and S6K). Taken together, these data reveal a role for PRC2 in maintaining human NPCs

in a proliferative state throughout cortical development, thus ensuring appropriate neuronal output and cortical organoid size (Figure 4J).

Inhibition of PRC2 induces changes in H3K27 methylation and acetylation

To explore whether inhibition of PRC2 affects other histone modifications, in addition to H3K27me3, we used our large-scale Epi-CyTOF approach on inhibitor-treated human cortical organoids (Figure 5A). Clustering of cell populations based on SOX2/PAX6, TBR2, and CTIP2 staining identified similar cell populations in DMSO and EEDi conditions, with strong KI67 expression in the NPC populations (Figures 5B and 5C). Epi-CyTOF confirmed the near-complete loss of H3K27me3 after EEDi treatment (Figures 5D and 5E; Table S4). Likewise, H3K27me2 was lost, whereas H3K27me1 was increased in neurons (Figures 5F and 5G). In agreement with previous reports, 42,43 the loss of H3K27me2/3 was accompanied by a gain of H3K27ac in all three neural cell populations. In contrast, PRC1-mediated H2AK119ub1 remained unchanged after PRC2 inhibition, which is in agreement with PRC1-independent targeting of PRC2 to chromatin. ¹⁷ None of the other histone modifications displayed global changes in their levels, including H3K4me2/3. This analysis demonstrates the power of the Epi-CyTOF technology to detect epigenetic changes across a large panel of histone modifications in specific cell populations isolated from complex tissues, such as human cortical organoids.

H3K27me3 is enriched on neuronal differentiation and ECM genes

Identification of PRC2 as a regulator of human NPC cell fate decisions led us to ask which genes were modified by H3K27me3 and how these targets might mediate the phenotypes observed upon PRC2 inhibition. Analysis of cell-typespecific PRC2 targets in the human fetal neocortex (Figure 6A) revealed a higher number of H3K27me3-binding sites in neurons compared with RG and IPs (Figure 6B). This was reflected in a higher number of significantly enriched neuron-specific target regions (Figure 6C). Plotting of the average coverage revealed that neuron-specific target regions, while more abundant, displayed lower enrichment of H3K27me3 compared with NPC-specific targets (Figures 6D and 6E). NPC-specific target regions showed a strong depletion of H3K27me3 upon differentiation. In contrast, neuronspecific targets acquired comparably lower levels of the repressive mark.

To examine the function of the cell-type-specific PRC2 targets, we annotated each region to its nearest neighboring gene and performed pathway analysis. 44 As expected, in NPCs, PRC2 was found to regulate genes associated with neuronal differentiation processes (Figure 6F). In addition, pathway analysis pointed toward secreted signaling molecules, including netrins and their receptors (Table S3). Moreover, in neurons, PRC2 target genes were linked to ECM organization and ECM interactions (Figure 6G). These findings are especially interesting considering previous results from mice, where cortex-specific knockout of *Eed* led to changes in the neurogenic differentiation of NPCs only upon tissue-wide knockout, but not upon deletion of *Eed* in



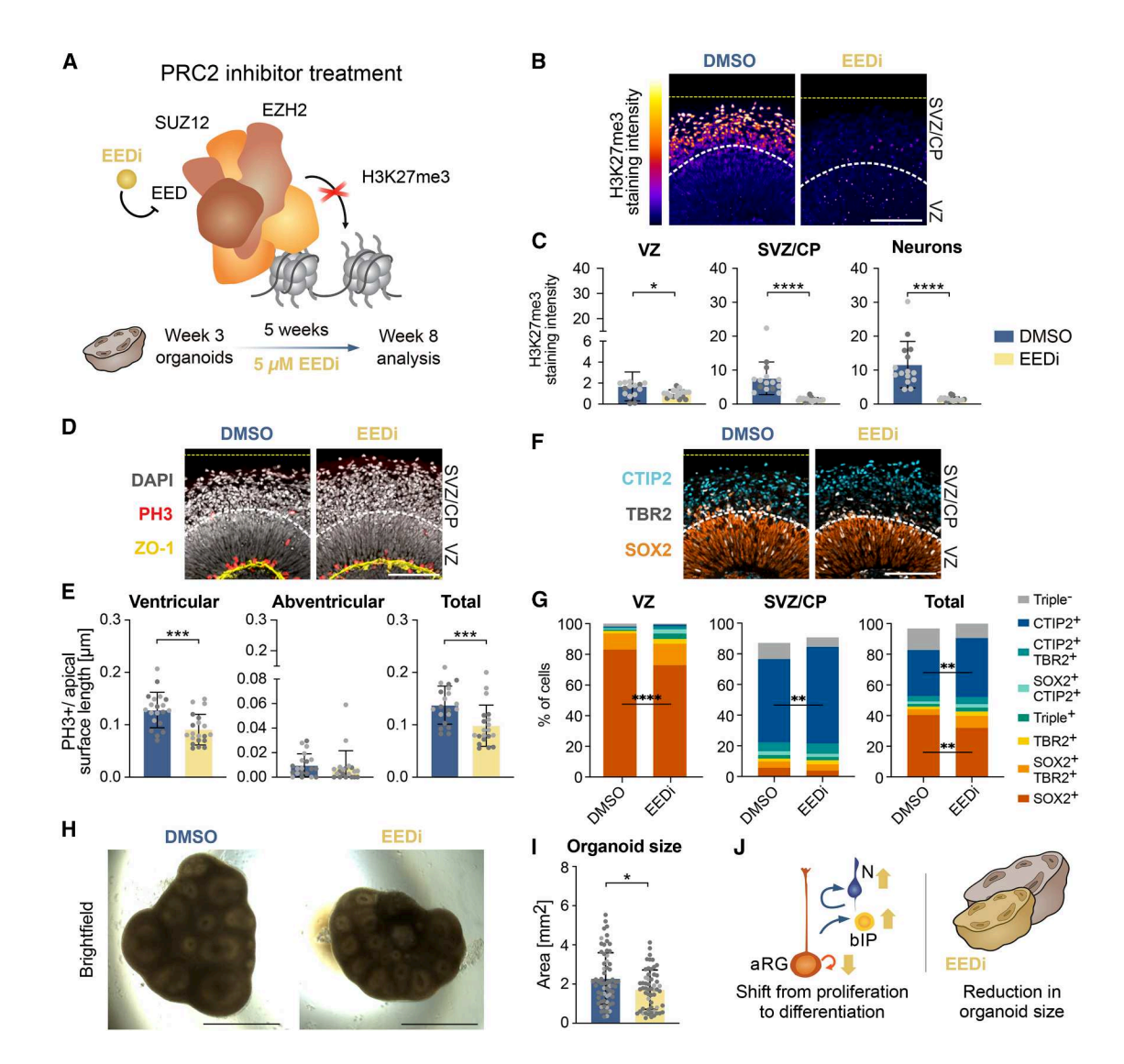


Figure 4. Inhibition of PRC2 results in a shift of NPC proliferation to differentiation

- (A) Experimental scheme for inhibition of PRC2.
- (B) Immunofluorescence of H3K27me3.
- (C) Quantification of H3K27me3 staining intensity in nuclei (segmented using DAPI) of VZ, SVZ/CP, and CTIP2-positive neurons.
- (D) DAPI staining and immunofluorescence of the apical surface marker ZO-1 and mitotic marker PH3.
- (E) Quantification of PH3⁺ cells per apical surface length (determined by ZO-1 signal) in ventricular (up to three nuclei away from the apical surface), abventricular, and total area.
- (F) Immunofluorescence of SOX2, TBR2, and CTIP2.
- (G) Quantification of SOX2, TBR2, and CTIP2 as percentage of total cells.
- (H) Brightfield images of cortical organoids treated with EEDi (W8).
- (I) Quantification of total organoid size.
- (J) Summary scheme of phenotypes.

Scale bars, (B, D, F) 100 μ m, (H) 1 mm. Bar graphs represent mean values. Error bars represent SD; (C), of 17–19 ventricles from at least 10 organoids; (D), of 18–20 ventricles from at least 10 organoids; (G), of 12 ventricles from at least 8 organoids; (I), of 56–63 organoids from 2 organoid batches (indicated by different colors). ****p < 0.001, ***p < 0.001, ***p < 0.001, and *p < 0.05; Kruskal-Wallis test with Dunn's post hoc test (C and E), two-way (G) or one-way (I) ANOVA with Tukey's post hoc test.

individual cells in an otherwise wild-type tissue.²¹ These results suggest a non-cell-autonomous mechanism for the regulation of NPC fate decisions by PRC2.

Among the genes marked by H3K27me3 in a cell-type-specific manner and encoding signaling molecules or ECM compo-

nents was *Unc-5 netrin receptor A (UNC5A)* (Figures 6H and 6I). This NPC-specific target gene was marked by H3K27me3 in RG and IPs and became activated in neurons. Netrin signaling has been described to direct cell migration and axon migration in the developing brain, ⁴⁵ thus regulating tissue morphology and





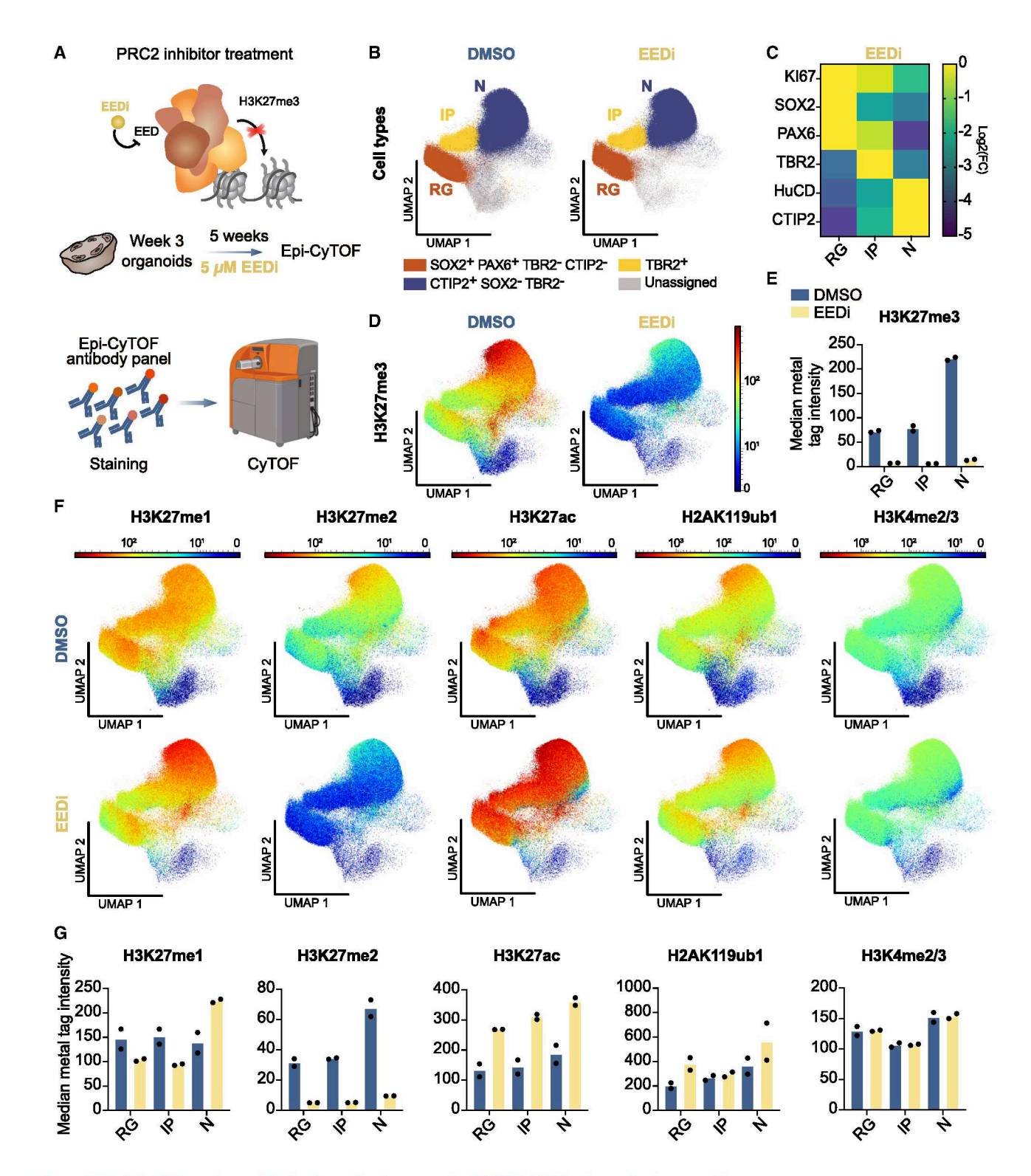


Figure 5. Epi-CyTOF resolves global epigenetic changes after PRC2 inhibition in cortical organoids

(A) Experimental workflow.

(legend continued on next page)

⁽B) UMAP analysis of cell-type clustering for DMSO- and EEDi-treated cortical organoids.

⁽C) Heatmap of log2 fold changes (FCs) of median metal tag intensities (2 replicates from independent batches).





structure. Among the neuron-specific PRC2 target genes, we identified different syndecans, which are cell surface proteogly-cans that regulate neural stem cell proliferation. 46,47 Specifically, *Syndecan 2 (SDC2)* was expressed in RG but was downregulated and enriched in H3K27me3 in neurons (Figures 6J and 6K).

Taken together, rather than only targeting neuronal differentiation genes, PRC2 might have a secondary mechanism of action by regulating ECM components. This may contribute to the localized enrichment of pro-proliferative ECM factors in the germinal zones, thus potentially maintaining NPC proliferative capacity through a non-cell-autonomous process.

PRC2 inhibition results in changes in ECM gene regulation and expression in cortical organoids

To evaluate the effect of PRC2 inhibition on histone methylation at target genes, we performed cell-type-specific CUT&Tag for H3K27me3 and H3K4me2/3 of EEDi-treated organoids (Figure 7A). This confirmed our results obtained by immunohistochemistry analysis (Figures 4B and 4C) and Epi-CyTOF (Figures 5D and 5E), revealing an essentially complete loss of H3K27me3 at previously enriched regions (Figure 7B). As a result, RG, IPs and neurons were found clustered together in PCA analysis of H3K27me3 after EEDi treatment of organoids, whereas for DMSO control samples, RG and IPs were closer together, but separate from neurons (Figure 7C), as also observed for human fetal tissue (Figure 3D). Overall, we saw a very strong depletion of H3K27me3 in the EEDi versus DMSO control condition (Figure 7D), with 28,241 regions showing a significant loss of H3K27me3 (Figure 7E). Notably, loss of H3K27me3 had no significant effect on H3K4me2/3 profiles (Figures S7A-S7C).

Next, we associated the regions that were sensitive to H3K27me3 loss with their predicted target genes. Despite the majority of H3K27me3 being lost, the most strongly enriched pathways were related to neuronal systems and ECM organization (Figure 7F). Interestingly, typical terms associated with Polycomb regulation, such as genes related to the development of other organs (heart, digestive tract, and skeletal system), 18,24 were not enriched. Among the terms associated with the extracellular environment, collagen formation, integrin cell surface interactions, ECM degradation, and Netrin-1 signaling are noteworthy. All these terms point to a role of PRC2 target genes in remodeling the extracellular niche during human cortical development.

To investigate the effects of H3K27me3 depletion on gene expression, we performed RNA sequencing (RNA-seq) for FANS-isolated RG, IPs, and neurons from the DMSO and EEDi conditions after 5 weeks of treatment in W8 human cortical organoids. Overall, the effects on gene expression were small, and after EEDi treatment, the RG, IP, and neuron cell populations clustered with the DMSO control samples (Figure S7D). In line with the repressive function of PRC2, we mostly detected upregulated genes in all cell types (Figure S7E; Table S5). A total of 18

genes were significantly upregulated across all cell types, and upregulated genes were associated with synapse function (Figure S7F). We reasoned that at W8, after 5 weeks of treatment, gene expression may have reached an equilibrium through compensatory mechanisms, and therefore also examined gene expression by RNA-seq of whole organoids after 2 weeks of EEDi treatment. This revealed more differentially expressed genes, specifically 131 upregulated and 3 downregulated genes in EEDi compared with the control condition (Figures S7G and S7H; Table S6). Pathway analysis indicated that most upregulated genes were associated with synapse function (Figure S7I). In addition, we identified the Gene Ontology terms "collagen-containing ECM" (Figure S7I) and "ECM structural constituent" (p adjust. 2.47e-02). Finally, we performed pathway analysis on previously published RNA-seg data²¹ of mouse Eed conditional knockout at E16, among which we found several ECM-related terms for upregulated genes (Figures S7J-S7M; Table S7), suggesting that the mechanism of PRC2-mediated regulation of the extracellular niche is conserved between mouse and human.

In summary, overall, the effects on gene expression were relatively small, in line with early embryonic development being the most critical period of PRC2 function. ^{24,48–51} After PRC2 inhibition during cortical development, we observed a shift of NPC fate from proliferation to differentiation, which is highly dependent on the extracellular niche of the human developing neocortex. ^{52,53} In line with this, we observed PRC2-mediated H3K27me3 at many ECM genes and found ECM-related pathways enriched among upregulated genes after PRC2 inhibition.

PRC2 inhibition results in aberrant ECM production in cortical organoids

We therefore examined differences in ECM-related factors at the protein level. The heparan sulfate proteoglycan Syndecan 1, which displayed a high enrichment of H3K27me3 in neurons (Figure 8A), was significantly enriched in both the VZ and SVZ/CP of EEDi-treated organoids compared with the DMSO control (Figures 8B and 8C). Moreover, the *LAMA1* gene was marked by H3K27me3 in neurons, which was lost upon EEDi treatment (Figure 8D). This gene codes for the laminin alpha 1 (LAMA1) chain of laminins, a family of ECM glycoproteins that regulate NPC proliferation and differentiation in mouse and human. ⁵³ In EEDi-treated cortical organoids, LAMA1 protein levels were also increased in the SVZ/CP (Figures 8E and 8F), further supporting the role of PRC2 in regulating the ECM composition in human cortical development.

To directly test whether adding ECM components affects human corticogenesis, we treated human cortical organoids with ECM proteins. Treatment of human cortical organoids with single ECM components, specifically Syndecan 1 or Syndecan 2, did not result in changes in the number of mitotic cells (Figures S8A–S8C). Since prolonged treatment with ECM

⁽D) Color-continuous scatter plots of H3K27me3. Scale represents metal isotope tag intensity.

⁽E) Median metal tag intensities of H3K27me3.

⁽F) Color-continuous scatter plots.

⁽G) Median metal tag intensities.





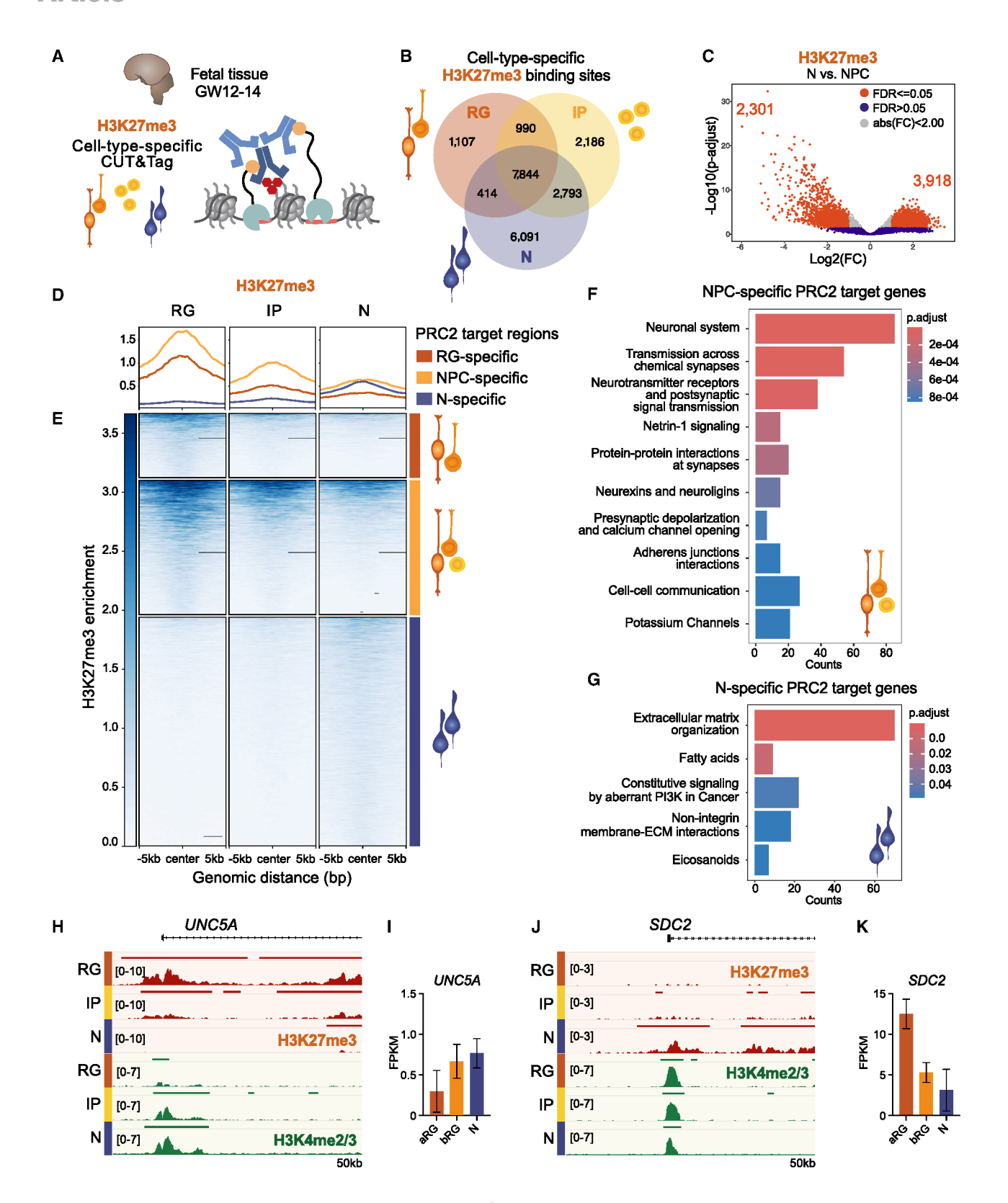


Figure 6. H3K27me3 is enriched on neuronal differentiation and ECM genes

(A) Experimental scheme for cell-type-specific CUT&Tag.

(B) Venn diagram showing the overlap of H3K27me3-binding sites in RG, IP, and N.



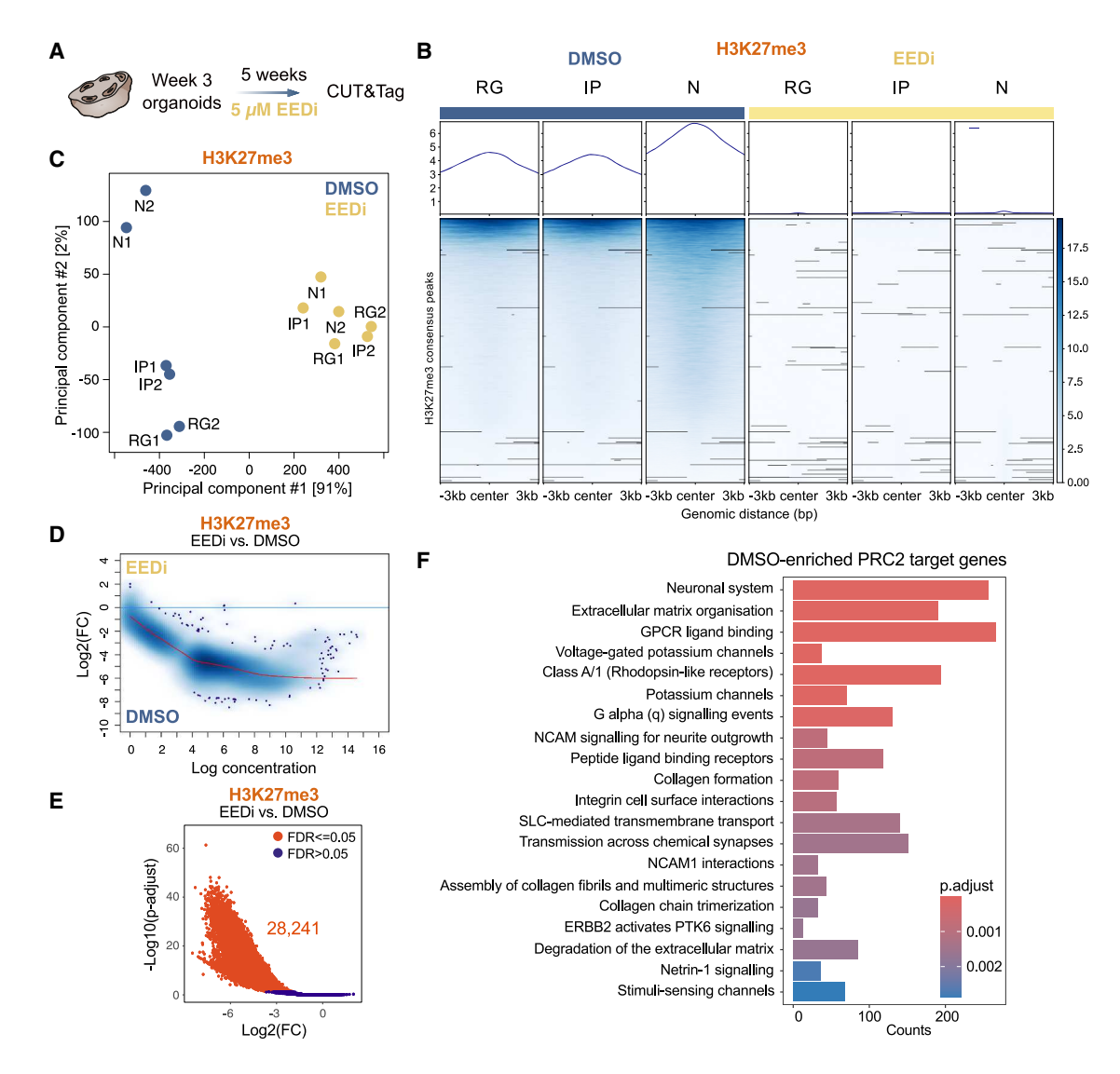


Figure 7. PRC2 inhibition results in changes in ECM gene regulation and expression in cortical organoids

- (A) Experimental scheme for CUT&Tag analysis following inhibition of PRC2.
- (B) Profiles and heatmaps of the enrichment of H3K27me3 in cortical organoids treated with EEDi or DMSO in a set of consensus peaks (mean of two independent organoid batches).
- (C) PCA analysis for cell-type-specific H3K27me3. Each dot presents a cell type from an independent organoid batch.
- (D) MA plot illustrating differential enrichment of H3K27me3 between EEDi and DMSO control condition.
- (E) Volcano plot displaying regions of differential H3K27me3 enrichment between EEDi and DMSO control condition (red; p adjust. < 0.05; log2FC > 1).
- (F) Reactome pathway enrichment for DMSO-enriched PRC2 target genes.

proteins may be buffered by ECM-degrading enzymes, we next turned to mouse hemisphere rotation cultures, which we had previously successfully used to assess the function of secreted factors on NPC proliferation after only 1 day of culture. ⁵² Also in the mouse, the addition of Syndecan 1 or Syndecan 2 did not alter the number of mitotic cells (Figures S8D–S8F). However,

⁽C) Volcano plot displaying regions of differential H3K27me3 enrichment between N and NPC (combining RG and IP). Significantly enriched regions are in red (p adjust. < 0.05; log2FC > 1).

⁽D and E) Profiles (D) and heatmaps (E) of the H3K27me3 enrichment of PRC2 target regions (average of 2 samples).

⁽F and G) Reactome pathway enrichment for PRC2 target genes.

⁽H) Tracks of H3K27me3 and H3K4me2/3 at the UNC5A genomic locus.

⁽I) Corresponding UNC5A mRNA in human fetal cortex (data from Florio et al. 35).

⁽J) Tracks of H3K27me3 and H3K4me2/3 at the SDC2 genomic locus.

⁽K) SDC2 mRNA levels.





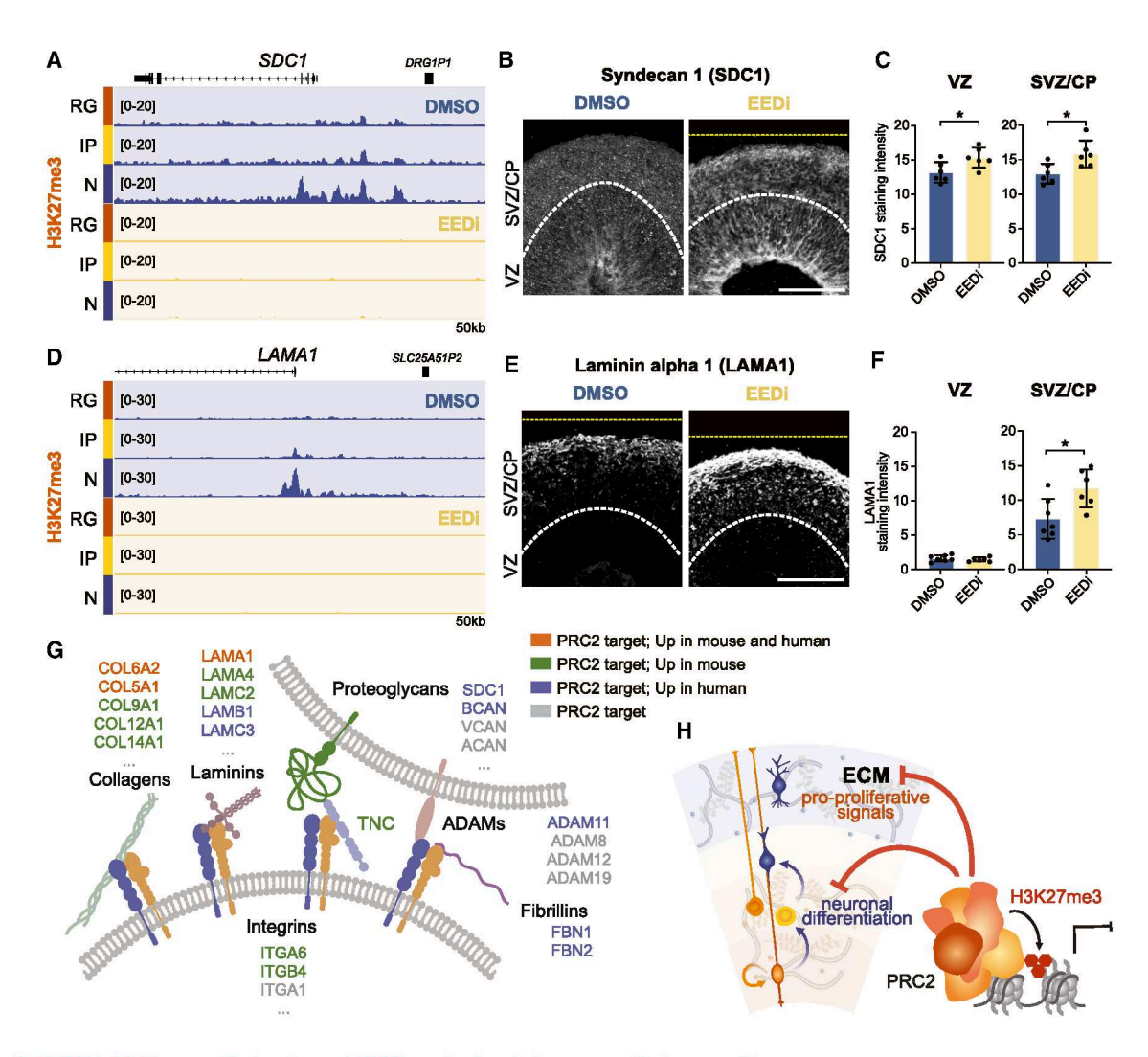


Figure 8. PRC2 inhibition results in aberrant ECM production in human cortical organoids

- (A) Tracks of H3K27me3 at the SDC1 genomic locus.
- (B) Immunofluorescence for SDC1 in cortical organoids from DMSO and EEDi treatment conditions.
- (C) Quantification of SDC1 staining intensity.
- (D) Tracks of H3K27me3 at the LAMA1 genomic locus.
- (E) Immunofluorescence for LAMA1.
- (F) Quantification of LAMA1 staining intensity.
- (G) Example ECM genes that are marked by H3K27me3 in the human developing neocortex and upregulated in mouse²¹ and/or human cortical development following PRC2 deletion or inhibition, respectively.
- (H) Model of the role of PRC2 function in human cortical development.

Scale bars, 100 µm. Bar graphs represent mean values. Error bars represent SD of 6-7 ventricles from at least 3 organoids. *p < 0.05; two-tailed unpaired t test.

both the analysis of PRC2 target genes and gene expression changes indicated that many different ECM components were regulated by PRC2 (Figure 8G), suggesting that the addition of one individual ECM component likely is not sufficient to recapitulate the changes in NPC proliferation and differentiation observed after EEDi treatment. Integrin receptors represent important receptors for ECM components. ECM-mediated changes in NPC proliferation were previously shown to be mediated by integrin signaling. Therefore, we next treated mouse hemisphere rotation cultures with an integrin $\beta 1$ blocking antibody, which, as previously described, 56 resulted in an in-

crease in the number of abventricular PH3-positive cells after 24 h (Figures S8G and S8H). Interestingly, this increase in abventricular mitotic cells depended on PRC2 function and was not observed after EEDi inhibition, strengthening the link between PRC2 function and ECM signaling.

Taken together, analysis of Syndecan 1 and LAMA1 protein levels further supported the conclusion that PRC2 contributes to shaping the ECM composition. Our findings, thus, reveal a potential mechanism for non-cell-autonomous functions of PRC2 in cortical development, by regulating genes involved in the secretion of signaling molecules and the composition of the ECM in





the extracellular niche of the developing neocortex, in which RG, IPs, and neurons reside (Figure 8H).

DISCUSSION

Our study employed a highly multiplexed approach to explore a large number of histone modifications at single-cell level in the human developing neocortex, providing unprecedented insights into global changes of epigenetic states during human neurogenesis. Functional experiments revealed that PRC2 regulates the transition of human NPCs from proliferation to differentiation, which is a key determinant of cortical size. Epigenome analysis identified ECM components as major targets of PRC2-mediated H3K27me3 in the human developing neocortex, raising the intriguing possibility that PRC2 non-cell autonomously regulates cell fate by modulating the composition of the extracellular stem cell niche in the developing brain.

Epi-CyTOF represents a large-scale method to detect cell-type-specific epigenetic changes

Despite recent advances in single-cell epigenomics, studying the many layers of histone posttranslational modifications has remained challenging in complex tissues, limiting our understanding of the epigenetic regulation of neural cell fate decisions, especially in human. Typically, global histone modification levels are assessed by western blotting, 48,57,58 despite the low throughput of the method and limited applicability to tissues that are composed of multiple cell types. CyTOF is a powerful method that takes advantage of metal-conjugated antibodies to quantify proteins within single cells. While well established in immunology, hematology, and oncology, 59,60 CyTOF was only recently applied to study chromatin modifications. ^{29,30} To adopt this powerful method for epigenetic studies of human brain development, we have established a custom Epi-CyTOF antibody panel consisting of >30 epigenetic readouts and 10 neural cell-type markers for the identification of major neural cell populations in the human developing neocortex.

In the future, Epi-CyTOF can be applied to identify global epigenetic changes in human neurodevelopmental disorders caused by mutations in epigenetic factors. ^{22,23} Here, we present proof-of-principle Epi-CyTOF data from EEDi inhibitor-treated cortical organoids. Knowledge of the complexity and interplay of epigenetic alterations has the potential to inform strategies to reverse epigenetic changes. The epigenome is crucial for higher cognitive functions, including memory and learning, and was reported to be dysregulated in neurodegenerative diseases and in aging. ^{61,62} Since epigenetic modifications are reversible, they represent promising targets for therapeutic intervention.

Preservation of epigenetic states in human organoid models of the developing brain

Transcriptome studies suggest that organoids preserve gene regulatory networks and developmental processes, even though metabolic differences were detected. 63–66 Less is known about the preservation of epigenomic features. Genome-wide analysis of DNA methylation suggested that most epigenomic features were recapitulated *in vitro*, even though DNA demethylation

occurred in pericentric repeat regions.⁶⁷ Additionally, emerging evidence suggests that chromatin modifications are maintained in forebrain organoids.^{68,69} Here, we showed that cell-type-specific patterns of a large number of histone posttranslational modifications were highly similar in human fetal tissue and human cortical organoids. Moreover, genome-wide distribution of H3K4me2/3 and H3K27me3, two modifications that are centrally involved in cell fate determination, ^{16,17} was recapitulated *in vitro*. This represents an important basis for the future application of brain organoid models in the investigation of epigenetic regulation in neurodevelopmental disorders.^{22,23} Specifically, mutations in the epigenetic factors regulating H3K4me2/3 and H3K27me3 levels are known to cause Kabuki and Weaver syndrome, two developmental disorders characterized by changes in brain size and intellectual disability.^{22,23}

PRC2 regulates genes that shape the extracellular environment of the human developing neocortex

Recently, brain organoid models revealed a role of PRC2 in regulating the exit from pluripotency²⁴ and the timing of neuronal maturation,²⁵ which represents a highly protracted process in humans.^{40,70} In addition, we show here that PRC2 also regulates the timing during early human cortical development, specifically by controlling the neural cell fate progression from RG to IPs to neurons

We identified ECM components and signaling molecules as PRC2 targets, both of which shape the stem cell niche in the human developing neocortex.53,71 We and others have previously proposed that human RG maintain the SVZ as a proliferative niche by locally producing ECM and growth factors to activate self-renewal pathways. 35,52,72-74 Mutations in ECM genes cause neurodevelopmental disorders,53 and recent evidence suggests that human LIS1 organoid disease models display altered ECM composition with changes in tissue viscoelastic properties.⁷⁵ Here, we found that epigenetic mechanisms contribute to the regulation of ECM genes. Even small changes in the composition of the extracellular environment may alter the propensity of NPCs for proliferation, as suggested by evolutionary studies.⁵² This provides a mechanistic explanation of previous findings that revealed a role of PRC2 at the global tissue-wide level in the mouse developing brain, rather than a cell-autonomous requirement in neurogenic RG.²¹

Overall, our findings suggest that in addition to the cell-autonomous regulation of neurogenic genes, epigenetic regulation of ECM genes may contribute to the determination of neural cell fate in the human developing neocortex by shaping the composition of the stem cell niche.

Limitations of the study

The Epi-CyTOF approach involves a panel of antibodies directed toward different epigenetic marks. Even though most antibodies against histone posttranslational modifications are well characterized, cross-reactivities to other modifications have been reported. Independent validation using alternative antibodies or specific inhibitors of epigenetic enzymes⁷⁶ is recommended for key findings. The cell-type marker panel may be modified to include other cell types that are present in the developing brain, such as endothelial cells, oligodendrocytes, and microglia. The suspension





mass cytometry technique applied here allows for the resolution of neural cell types, while spatial information regarding the location of the cells within the tissue is lost. This limitation may be overcome in the future by applying imaging-mass cytometry (IMC)-based analysis. 77 Organoids have become an important tool for studies of human brain development, despite known limitations, such as the reduced expansion of the outer SVZ and limited development of neuronal layers. Therefore, we have included primary fetal tissue in this study, which serves as an important reference for the epigenetic state *in vivo*.

RESOURCE AVAILABILITY

Lead contact

Requests for further information should be directed to and will be fulfilled by the lead contact, Mareike Albert (mareike.albert@tu-dresden.de).

Materials availability

This study did not generate new unique reagents. All iPSC lines were previously published. The human iPSC line CRTDi004-A is available via the lead contact from the CMCB Stem Cell Engineering Facility subject to institutional MTA regulations.

Data and code availability

De-identified human CUT&Tag sequencing data have been deposited at Zenodo: https://doi.org/10.5281/zenodo.13897222. Human Epi-CyTOF data have been deposited at FlowRepository: http://flowrepository.org (Repository ID: FR-FCM-Z8DC). This paper analyses existing, publicly available data, accessible at GEO as GEO: GSE65000. All original code has been deposited at Zenodo and is publicly available (Zenodo: https://doi.org/10.5281/zenodo. 13897222).

ACKNOWLEDGMENTS

We are grateful to the facilities of the CRTD and Dresden Concept partners for the outstanding support provided, notably K. Neumann and the Stem Cell Engineering Facility, H. Hartmann and the Light Microscopy Facility, A. Gompf and at the Flow Cytometry Facility, and S. Weiche from histology and the wet-lab team at the Dresden Concept Genome Center. We thank all members of the Albert laboratory for their help and discussions. We acknowledge the Wellcome Trust Sanger Institute (HipSci) for providing the HPSI0114i-kolf_2 iPSC line. M.A. acknowledges funding from the Center for Regenerative Therapies TU Dresden (CRTD), the DFG (Emmy Noether, AL 2231/1-1), the Schram Foundation, the ERA-NET Neuron (MEPIcephaly; Federal Ministry of Research, Technology and Space [BMRTS], 01EW2208), and the Fritz Thyssen Foundation. F.B., A.E., M.O.K., and M.A. acknowledge support from the German Centers for Health Research (DZG). K.S. was supported by the DFG Research Infrastructure NGS_CC (INST 269/468-1 and INST 269/768-1, project 407482635, DcGC DRESDEN-Concept Genome Center). This work was supported by the Mass Cytometry Core Facility at the CRTD. Ezio Bonifacio (CRTD) raised funding from the DFG (FZT 111) to purchase the suspension mass cytometer CyTOF 2 and from the BMBF to the German Center for Diabetes Research (DZD e.V.) to purchase the suspension mass cytometer CvTOF XT together with the Medical Faculty Carl Gustay Carus, TU Dresden. and the Staatsministerium für Wissenschaft, Kultur und Tourismus (SMWK), Germany.

AUTHOR CONTRIBUTIONS

Conceptualization, N.D., E.S., and M.A.; investigation, N.D., E.S., A.K., T.M.S., A.N., K.K., S.D., and C.P.; resources, A.K., T.M.S., K.S., R.P.D., C.B., A.D., and P.W.; formal analysis, N.D., E.S., K.K., and A.K.; visualization, N.D. and E.S.; writing – original draft, N.D., E.S., and M.A.; writing – review & editing, N.D., E.S., A.K., T.M.S., A.N., K.K., C.P., and M.A.; funding acquisition, A.E., M.O.K., F.B., and M.A.; supervision, M.A.

DECLARATION OF INTERESTS

The authors declare no competing interests.

DECLARATION OF GENERATIVE AI AND AI-ASSISTED TECHNOLOGIES IN THE WRITING PROCESS

During the preparation of this work, the authors used Grammarly for spelling and grammar checks. After using the tool, the authors reviewed and edited the content as needed and take full responsibility for the content of the publication.

STAR*METHODS

Detailed methods are provided in the online version of this paper and include the following:

- KEY RESOURCES TABLE
- EXPERIMENTAL MODEL AND SUBJECT DETAILS
 - o Human fetal tissue
 - o Human induced pluripotent stem cell lines
 - Mic
- METHOD DETAILS
 - o Cortical organoid culture
 - o Mouse hemisphere rotation culture
 - o Metal isotope conjugation of antibodies
 - o Tissue dissociation for Epi-CyTOF
 - o Palladium-based barcoding and cell staining for Epi-CyTOF
 - CvTOF measurement
 - Epi-CyTOF data analysis
 - $\ \, \circ \ \, \text{Immunofluorescence staining} \\$
 - o Image analysis
 - Isolation of neural cell populations for CUT&Tag and RNA-seq
 - $\circ\,$ Gene expression analysis by RT-qPCR
 - CUT&Tag library preparation
 - CUT&Tag data analysis
 - o RNA-seq library preparation
 - O RNA-seq data analysis
 - Statistical analysis

SUPPLEMENTAL INFORMATION

Supplemental information can be found online at https://doi.org/10.1016/j.neuron.2025.06.016.

Received: November 6, 2024 Revised: May 22, 2025 Accepted: June 23, 2025 Published: July 22, 2025

REFERENCES

- Lui, J.H., Hansen, D.V., and Kriegstein, A.R. (2011). Development and evolution of the human neocortex. Cell 146, 18–36. https://doi.org/10. 1016/j.cell.2011.06.030.
- Florio, M., and Huttner, W.B. (2014). Neural progenitors, neurogenesis and the evolution of the neocortex. Development 141, 2182–2194. https://doi.org/10.1242/dev.090571.
- Borrell, V., and Reillo, I. (2012). Emerging roles of neural stem cells in cerebral cortex development and evolution. Dev. Neurobiol. 72, 955–971. https://doi.org/10.1002/dneu.22013.
- Pollen, A.A., Kilik, U., Lowe, C.B., and Camp, J.G. (2023). Human-specific genetics: new tools to explore the molecular and cellular basis of human evolution. Nat. Rev. Genet. 24, 687–711. https://doi.org/10.1038/s41576-022-00568-4.





- Nano, P.R., and Bhaduri, A. (2022). Evaluation of advances in cortical development using model systems. Dev. Neurobiol. 82, 408–427. https://doi.org/10.1002/dneu.22879.
- Vanderhaeghen, P., and Polleux, F. (2023). Developmental mechanisms underlying the evolution of human cortical circuits. Nat. Rev. Neurosci. 24, 213–232. https://doi.org/10.1038/s41583-023-00675-z.
- Hoye, M.L., and Silver, D.L. (2021). Decoding mixed messages in the developing cortex: translational regulation of neural progenitor fate. Curr. Opin. Neurobiol. 66, 93–102. https://doi.org/10.1016/j.conb.2020. 10.001.
- Amberg, N., Laukoter, S., and Hippenmeyer, S. (2019). Epigenetic cues modulating the generation of cell-type diversity in the cerebral cortex. J. Neurochem. 149, 12–26. https://doi.org/10.1111/jnc.14601.
- Hirabayashi, Y., and Gotoh, Y. (2010). Epigenetic control of neural precursor cell fate during development. Nat. Rev. Neurosci. 11, 377–388. https://doi.org/10.1038/nrn2810.
- Albert, M., and Huttner, W.B. (2018). Epigenetic and transcriptional prepatterning-An emerging theme in cortical neurogenesis. Front. Neurosci. 12, 359. https://doi.org/10.3389/fnins.2018.00359.
- Yao, B., Christian, K.M., He, C., Jin, P., Ming, G.L., and Song, H. (2016).
 Epigenetic mechanisms in neurogenesis. Nat. Rev. Neurosci. 17, 537–549. https://doi.org/10.1038/nrn.2016.70.
- Millán-Zambrano, G., Burton, A., Bannister, A.J., and Schneider, R. (2022). Histone post-translational modifications cause and consequence of genome function. Nat. Rev. Genet. 23, 563–580. https://doi.org/10.1038/s41576-022-00468-7.
- Turner, B.M. (1993). Decoding the nucleosome. Cell 75, 5–8. https://doi. org/10.1016/S0092-8674(05)80078-9.
- Corley, M., and Kroll, K.L. (2015). The roles and regulation of Polycomb complexes in neural development. Cell Tissue Res. 359, 65–85. https:// doi.org/10.1007/s00441-014-2011-9.
- Tsuboi, M., Hirabayashi, Y., and Gotoh, Y. (2019). Diverse gene regulatory mechanisms mediated by Polycomb group proteins during neural development. Curr. Opin. Neurobiol. 59, 164–173. https://doi.org/10.1016/j. conb.2019.07.003.
- Piunti, A., and Shilatifard, A. (2016). Epigenetic balance of gene expression by Polycomb and COMPASS families. Science 352, aad9780. https://doi.org/10.1126/science.aad9780.
- Schuettengruber, B., Bourbon, H.M., Di Croce, L., and Cavalli, G. (2017).
 Genome regulation by Polycomb and Trithorax: 70 years and counting.
 Cell 171, 34–57. https://doi.org/10.1016/j.cell.2017.08.002.
- Albert, M., Kalebic, N., Florio, M., Lakshmanaperumal, N., Haffner, C., Brandl, H., Henry, I., and Huttner, W.B. (2017). Epigenome profiling and editing of neocortical progenitor cells during development. EMBO J. 36, 2642–2658. https://doi.org/10.15252/embj.201796764.
- Pereira, J.D., Sansom, S.N., Smith, J., Dobenecker, M.W., Tarakhovsky, A., and Livesey, F.J. (2010). Ezh2, the histone methyltransferase of PRC2, regulates the balance between self-renewal and differentiation in the cerebral cortex. Proc. Natl. Acad. Sci. USA 107, 15957–15962. https://doi. org/10.1073/pnas.1002530107.
- Telley, L., Agirman, G., Prados, J., Amberg, N., Fièvre, S., Oberst, P., Bartolini, G., Vitali, I., Cadilhac, C., Hippenmeyer, S., et al. (2019). Temporal patterning of apical progenitors and their daughter neurons in the developing neocortex. Science 364, eaav2522. https://doi.org/ 10.1126/science.aav2522.
- Amberg, N., Pauler, F.M., Streicher, C., and Hippenmeyer, S. (2022).
 Tissue-wide genetic and cellular landscape shapes the execution of sequential PRC2 functions in neural stem cell lineage progression. Sci. Adv. 8, eabq1263. https://doi.org/10.1126/sciadv.abq1263.
- Bölicke, N., and Albert, M. (2022). Polycomb-mediated gene regulation in human brain development and neurodevelopmental disorders. Dev. Neurobiol. 82, 345–363. https://doi.org/10.1002/dneu.22876.

- Mastrototaro, G., Zaghi, M., and Sessa, A. (2017). Epigenetic mistakes in neurodevelopmental disorders. J. Mol. Neurosci. 61, 590–602. https:// doi.org/10.1007/s12031-017-0900-6.
- Zenk, F., Fleck, J.S., Jansen, S.M.J., Kashanian, B., Eisinger, B., Santel, M., Dupré, J.S., Camp, J.G., and Treutlein, B. (2024). Single-cell epigenomic reconstruction of developmental trajectories from pluripotency in human neural organoid systems. Nat. Neurosci. 27, 1376–1386. https://doi.org/10.1038/s41593-024-01652-0.
- Ciceri, G., Baggiolini, A., Cho, H.S., Kshirsagar, M., Benito-Kwiecinski, S., Walsh, R.M., Aromolaran, K.A., Gonzalez-Hernandez, A.J., Munguba, H., Koo, S.Y., et al. (2024). An epigenetic barrier sets the timing of human neuronal maturation. Nature 626, 881–890. https://doi.org/10. 1038/s41586-023-06984-8.
- Noack, F., Vangelisti, S., Ditzer, N., Chong, F., Albert, M., and Bonev, B. (2023). Joint epigenome profiling reveals cell-type-specific gene regulatory programmes in human cortical organoids. Nat. Cell Biol. 25, 1873–1883. https://doi.org/10.1038/s41556-023-01296-5.
- Bartosovic, M., Kabbe, M., and Castelo-Branco, G. (2021). Single-cell CUT&Tag profiles histone modifications and transcription factors in complex tissues. Nat. Biotechnol. 39, 825–835. https://doi.org/10.1038/ s41587-021-00869-9.
- Meers, M.P., Llagas, G., Janssens, D.H., Codomo, C.A., and Henikoff, S. (2023). Multifactorial profiling of epigenetic landscapes at single-cell resolution using MulTI-Tag. Nat. Biotechnol. 41, 708–716. https://doi.org/10.1038/s41587-022-01522-9.
- Cheung, P., Vallania, F., Warsinske, H.C., Donato, M., Schaffert, S., Chang, S.E., Dvorak, M., Dekker, C.L., Davis, M.M., Utz, P.J., et al. (2018). Single-Cell chromatin modification profiling reveals increased epigenetic variations with aging. Cell 173, 1385–1397.e14. https://doi. org/10.1016/j.cell.2018.03.079.
- Harpaz, N., Mittelman, T., Beresh, O., Griess, O., Furth, N., Salame, T.M., Oren, R., Fellus-Alyagor, L., Harmelin, A., Alexandrescu, S., et al. (2022).
 Single-cell epigenetic analysis reveals principles of chromatin states in H3.3-K27M gliomas. Mol. Cell 82, 2696–2713.e9. https://doi.org/10. 1016/j.molcel.2022.05.023.
- Qian, X., Su, Y., Adam, C.D., Deutschmann, A.U., Pather, S.R., Goldberg, E.M., Su, K., Li, S., Lu, L., Jacob, F., et al. (2020). Sliced Human Cortical Organoids for Modeling Distinct Cortical Layer Formation. Cell Stem Cell 26, 766–781.e9. https://doi.org/10.1016/j.stem.2020.02.002.
- Giandomenico, S.L., and Lancaster, M.A. (2017). Probing human brain evolution and development in organoids. Curr. Opin. Cell Biol. 44, 36–43. https://doi.org/10.1016/j.ceb.2017.01.001.
- 33. Paşca, S.P. (2018). The rise of three-dimensional human brain cultures. Nature 553, 437–445. https://doi.org/10.1038/nature25032.
- Barth, T.K., and Imhof, A. (2010). Fast signals and slow marks: the dynamics of histone modifications. Trends Biochem. Sci. 35, 618–626. https://doi.org/10.1016/j.tibs.2010.05.006.
- Florio, M., Albert, M., Taverna, E., Namba, T., Brandl, H., Lewitus, E., Haffner, C., Sykes, A., Wong, F.K., Peters, J., et al. (2015). Human-specific gene ARHGAP11B promotes basal progenitor amplification and neocortex expansion. Science 347, 1465–1470. https://doi.org/10. 1126/science.aaa1975.
- Jain, P., Ballare, C., Blanco, E., Vizan, P., and Di Croce, L. (2020). PHF19
 mediated regulation of proliferation and invasiveness in prostate cancer
 cells. eLife 9, e51373. https://doi.org/10.7554/eLife.51373.
- Aquilino, M., Ditzer, N., Namba, T., and Albert, M. (2025). Epigenetic and metabolic regulation of developmental timing in neocortex evolution. Trends Neurosci. 48, 430–444. https://doi.org/10.1016/j.tins.2025.03.001.
- Kaya-Okur, H.S., Wu, S.J., Codomo, C.A., Pledger, E.S., Bryson, T.D., Henikoff, J.G., Ahmad, K., and Henikoff, S. (2019). CUT&Tag for efficient epigenomic profiling of small samples and single cells. Nat. Commun. 10, 1930. https://doi.org/10.1038/s41467-019-09982-5.



- Ahanger, S.H., Zhang, C., Semenza, E.R., Gil, E., Cole, M.A., Wang, L., Kriegstein, A.R., and Lim, D.A. (2024). Spatial 3D genome organization controls the activity of bivalent chromatin during human neurogenesis. Preprint at bioRxiv. https://doi.org/10.1101/2024.08.01.606248.
- Ciceri, G., and Studer, L. (2024). Epigenetic control and manipulation of neuronal maturation timing. Curr. Opin. Genet. Dev. 85, 102164. https:// doi.org/10.1016/j.gde.2024.102164.
- Qi, W., Zhao, K., Gu, J., Huang, Y., Wang, Y., Zhang, H., Zhang, M., Zhang, J., Yu, Z., Li, L., et al. (2017). An allosteric PRC2 inhibitor targeting the H3K27me3 binding pocket of EED. Nat. Chem. Biol. 13, 381–388. https://doi.org/10.1038/nchembio.2304.
- Jung, H.R., Pasini, D., Helin, K., and Jensen, O.N. (2010). Quantitative mass spectrometry of histones H3.2 and H3.3 in Suz12-deficient mouse embryonic stem cells reveals distinct, dynamic post-translational modifications at Lys-27 and Lys-36. Mol. Cell. Proteomics 9, 838–850. https://doi.org/10.1074/mcp.M900489-MCP200.
- Pasini, D., Malatesta, M., Jung, H.R., Walfridsson, J., Willer, A., Olsson, L., Skotte, J., Wutz, A., Porse, B., Jensen, O.N., and Helin, K. (2010). Characterization of an antagonistic switch between histone H3 lysine 27 methylation and acetylation in the transcriptional regulation of Polycomb group target genes. Nucleic Acids Res. 38, 4958–4969. https://doi.org/10.1093/nar/gkq244.
- Yu, G., and He, Q.Y. (2016). ReactomePA: an R/Bioconductor package for reactome pathway analysis and visualization. Mol. Biosyst. 12, 477–479. https://doi.org/10.1039/c5mb00663e.
- Moore, S.W., Tessier-Lavigne, M., and Kennedy, T.E. (2007). Netrins and their receptors. Adv. Exp. Med. Biol. 621, 17–31. https://doi.org/10.1007/ 978-0-387-76715-4_2.
- Mouthon, M.A., Morizur, L., Dutour, L., Pineau, D., Kortulewski, T., and Boussin, F.D. (2020). Syndecan-1 Stimulates Adult Neurogenesis in the Mouse Ventricular-Subventricular Zone after Injury. iScience 23, 101784. https://doi.org/10.1016/j.isci.2020.101784.
- 47. Wang, Q., Yang, L., Alexander, C., and Temple, S. (2012). The niche factor syndecan-1 regulates the maintenance and proliferation of neural progenitor cells during mammalian cortical development. PLoS One 7, e42883. https://doi.org/10.1371/journal.pone.0042883.
- Pasini, D., Bracken, A.P., Hansen, J.B., Capillo, M., and Helin, K. (2007). The polycomb group protein Suz12 is required for embryonic stem cell differentiation. Mol. Cell. Biol. 27, 3769–3779. https://doi.org/10.1128/ MCB.01432-06.
- Boyer, L.A., Plath, K., Zeitlinger, J., Brambrink, T., Medeiros, L.A., Lee, T.I., Levine, S.S., Wernig, M., Tajonar, A., Ray, M.K., et al. (2006). Polycomb complexes repress developmental regulators in murine embryonic stem cells. Nature 441, 349–353. https://doi.org/10.1038/nature04733
- Pasini, D., Bracken, A.P., Jensen, M.R., Lazzerini Denchi, E., and Helin, K. (2004). Suz12 is essential for mouse development and for EZH2 histone methyltransferase activity. EMBO J. 23, 4061–4071. https://doi.org/10. 1038/si.emboj.7600402.
- O'Carroll, D., Erhardt, S., Pagani, M., Barton, S.C., Surani, M.A., and Jenuwein, T. (2001). The polycomb-group gene Ezh2 is required for early mouse development. Mol. Cell. Biol. 21, 4330–4336. https://doi.org/10. 1128/MCB.21.13.4330-4336.2001.
- Cubillos, P., Ditzer, N., Kolodziejczyk, A., Schwenk, G., Hoffmann, J., Schütze, T.M., Derihaci, R.P., Birdir, C., Köllner, J.E., Petzold, A., et al. (2024). The growth factor EPIREGULIN promotes basal progenitor cell proliferation in the developing neocortex. EMBO J. 43, 1388–1419. https://doi.org/10.1038/s44318-024-00068-7.
- Long, K.R., and Huttner, W.B. (2021). The Role of the Extracellular Matrix in Neural Progenitor Cell Proliferation and Cortical Folding During Human Neocortex Development. Front. Cell. Neurosci. 15, 804649. https://doi. org/10.3389/fncel.2021.804649.

- Fietz, S.A., Kelava, I., Vogt, J., Wilsch-Bräuninger, M., Stenzel, D., Fish, J. L., Corbeil, D., Riehn, A., Distler, W., Nitsch, R., and Huttner, W.B. (2010). OSVZ progenitors of human and ferret neocortex are epithelial-like and expand by integrin signaling. Nat. Neurosci. 13, 690–699. https://doi. org/10.1038/nn.2553.
- Stenzel, D., Wilsch-Bräuninger, M., Wong, F.K., Heuer, H., and Huttner, W.B. (2014). Integrin ανβ3 and thyroid hormones promote expansion of progenitors in embryonic neocortex. Development 141, 795–806. https://doi.org/10.1242/dev.101907.
- Loulier, K., Lathia, J.D., Marthiens, V., Relucio, J., Mughal, M.R., Tang, S. C., Coksaygan, T., Hall, P.E., Chigurupati, S., Patton, B., et al. (2009). beta1 integrin maintains integrity of the embryonic neocortical stem cell niche. PLoS Biol. 7, e1000176. https://doi.org/10.1371/journal.pbio.1000176.
- Healy, E., Mucha, M., Glancy, E., Fitzpatrick, D.J., Conway, E., Neikes, H. K., Monger, C., Van Mierlo, G., Baltissen, M.P., Koseki, Y., et al. (2019).
 PRC2.1 and PRC2.2 Synergize to Coordinate H3K27 Trimethylation.
 Mol. Cell 76, 437–452.e6. https://doi.org/10.1016/j.molcel.2019.08.012.
- Wang, H., Fan, Z., Shliaha, P.V., Miele, M., Hendrickson, R.C., Jiang, X., and Helin, K. (2023). H3K4me3 regulates RNA polymerase II promoterproximal pause-release. Nature 615, 339–348. https://doi.org/10.1038/ s41586-023-05780-8.
- Korin, B., Dubovik, T., and Rolls, A. (2018). Mass cytometry analysis of immune cells in the brain. Nat. Protoc. 13, 377–391. https://doi.org/10. 1038/nprot.2017.155.
- Hartmann, F.J., and Bendall, S.C. (2020). Immune monitoring using mass cytometry and related high-dimensional imaging approaches. Nat. Rev. Rheumatol. 16, 87–99. https://doi.org/10.1038/s41584-019-0338-z.
- Hwang, J.Y., Aromolaran, K.A., and Zukin, R.S. (2017). The emerging field of epigenetics in neurodegeneration and neuroprotection. Nat. Rev. Neurosci. 18, 347–361. https://doi.org/10.1038/nrn.2017.46.
- Wang, K., Liu, H., Hu, Q., Wang, L., Liu, J., Zheng, Z., Zhang, W., Ren, J., Zhu, F., and Liu, G.H. (2022). Epigenetic regulation of aging: implications for interventions of aging and diseases. Signal Transduct. Target. Ther. 7, 374. https://doi.org/10.1038/s41392-022-01211-8.
- Camp, J.G., Badsha, F., Florio, M., Kanton, S., Gerber, T., Wilsch-Bräuninger, M., Lewitus, E., Sykes, A., Hevers, W., Lancaster, M., et al. (2015). Human cerebral organoids recapitulate gene expression programs of fetal neocortex development. Proc. Natl. Acad. Sci. USA 112, 15672–15677. https://doi.org/10.1073/pnas.1520760112.
- 64. He, Z., Dony, L., Fleck, J.S., Szałata, A., Li, K.X., Slišković, I., Lin, H., Santel, M., Atamian, A., Quadrato, G., et al. (2023). An integrated transcriptomic cell atlas of human neural organoids. Preprint at bioRxiv. https://doi.org/10.1101/2023.10.05.561097.
- 65. Velasco, S., Kedaigle, A.J., Simmons, S.K., Nash, A., Rocha, M., Quadrato, G., Paulsen, B., Nguyen, L., Adiconis, X., Regev, A., et al. (2019). Individual brain organoids reproducibly form cell diversity of the human cerebral cortex. Nature *570*, 523–527. https://doi.org/10.1038/s41586-019-1289-x.
- Pollen, A.A., Bhaduri, A., Andrews, M.G., Nowakowski, T.J., Meyerson, O.S., Mostajo-Radji, M.A., Di Lullo, E., Alvarado, B., Bedolli, M., Dougherty, M.L., et al. (2019). Establishing cerebral organoids as models of human-specific brain evolution. Cell 176, 743–756.e17. https://doi.org/10.1016/j.cell.2019.01.017.
- Luo, C., Lancaster, M.A., Castanon, R., Nery, J.R., Knoblich, J.A., and Ecker, J.R. (2016). Cerebral organoids recapitulate epigenomic signatures of the human fetal brain. Cell Rep. 17, 3369–3384. https://doi. org/10.1016/j.celrep.2016.12.001.
- Amiri, A., Coppola, G., Scuderi, S., Wu, F., Roychowdhury, T., Liu, F., Pochareddy, S., Shin, Y., Safi, A., Song, L., et al. (2018). Transcriptome and epigenome landscape of human cortical development modeled in organoids. Science 362, eaat6720. https://doi.org/10.1126/science. aat6720.





- Lewis, E.M.A., Kaushik, K., Sandoval, L.A., Antony, I., Dietmann, S., and Kroll, K.L. (2021). Epigenetic regulation during human cortical development: Seq-ing answers from the brain to the organoid. Neurochem. Int. 147, 105039. https://doi.org/10.1016/j.neuint.2021.105039.
- Wallace, J.L., and Pollen, A.A. (2024). Human neuronal maturation comes of age: cellular mechanisms and species differences. Nat. Rev. Neurosci. 25, 7–29. https://doi.org/10.1038/s41583-023-00760-3.
- Berto, G., Pravata, M.V., and Cappello, S. (2025). Cellular interplay in brain organoids: Connecting cell-autonomous and non-cell-autonomous mechanisms in neurodevelopmental disease. Curr. Opin. Neurobiol. 92, 103018. https://doi.org/10.1016/j.conb.2025.103018.
- Fietz, S.A., Lachmann, R., Brandl, H., Kircher, M., Samusik, N., Schröder, R., Lakshmanaperumal, N., Henry, I., Vogt, J., Riehn, A., et al. (2012). Transcriptomes of germinal zones of human and mouse fetal neocortex suggest a role of extracellular matrix in progenitor self-renewal. Proc. Natl. Acad. Sci. USA 109, 11836–11841. https://doi.org/10.1073/pnas. 1209647109
- Kalebic, N., and Huttner, W.B. (2020). Basal progenitor morphology and neocortex evolution. Trends Neurosci. 43, 843–853. https://doi.org/10. 1016/j.tins.2020.07.009.
- Pollen, A.A., Nowakowski, T.J., Chen, J., Retallack, H., Sandoval-Espinosa, C., Nicholas, C.R., Shuga, J., Liu, S.J., Oldham, M.C., Diaz, A., et al. (2015). Molecular identity of human outer radial glia during cortical development. Cell 163, 55–67. https://doi.org/10.1016/j.cell. 2015.09.004.
- Karlinski Zur, M., Bhattacharya, B., Solomonov, I., Ben Dror, S., Savidor, A., Levin, Y., Prior, A., Sapir, T., Harris, T., Olender, T., et al. (2025). Altered extracellular matrix structure and elevated stiffness in a brain organoid model for disease. Nat. Commun. 16, 4094. https://doi.org/10.1038/s41467-025-59252-w.
- Jin, Y., Liu, T., Luo, H., Liu, Y., and Liu, D. (2022). Targeting Epigenetic Regulatory Enzymes for Cancer Therapeutics: Novel Small-Molecule Epidrug Development. Front. Oncol. 12, 848221. https://doi.org/10. 3389/fonc.2022.848221.
- Kuett, L., Catena, R., Özcan, A., Plüss, A., Cancer Grand Challenges IMAXT Consortium, Schraml, P., Moch, H., de Souza, N., and Bodenmiller, B. (2022). Three-dimensional imaging mass cytometry for highly multiplexed molecular and cellular mapping of tissues and the tumor microenvironment. Nat. Cancer 3, 122–133. https://doi.org/10.1038/ s43018-021-00301-w.
- Völkner, M., Wagner, F., Steinheuer, L.M., Carido, M., Kurth, T., Yazbeck, A., Schor, J., Wieneke, S., Ebner, L.J.A., Del Toro Runzer, C., et al. (2022). HBEGF-TNF induce a complex outer retinal pathology with photore-ceptor cell extrusion in human organoids. Nat. Commun. 13, 6183. https://doi.org/10.1038/s41467-022-33848-y.
- Cheshire, C., West, C., Rönkkö, T., Patel, H., Hodgetts, T., Ladd, D., Thiery, A., Fields, C., Deu-Pons, J., et al.; nf-core bot (2024). nf-core/cutandrun: nf-core/cutandrun v3.2.2 Iridium Ibis. Zenodo. https://doi.org/10.5281/zenodo.10606804.
- Stark, R., and Brown, G. (2012). DiffBind: Differential Binding Analysis of ChIP-Seq Peak Data. Bioconductor. https://www.bioconductor.org/ packages//2.10/bioc/vignettes/DiffBind/inst/doc/DiffBind.pdf.
- Love, M.I., Huber, W., and Anders, S. (2014). Moderated estimation of fold change and dispersion for RNA-seq data with DESeq2. Genome Biol. 15, 550. https://doi.org/10.1186/s13059-014-0550-8.
- Yu, G., Wang, L.G., and He, Q.Y. (2015). ChlPseeker: an R/Bioconductor package for ChlP peak annotation, comparison and visualization. Bioinformatics 31, 2382–2383. https://doi.org/10.1093/bioinformatics/ btv145.
- 83. Bioconductor Core Team; Bioconductor Package Maintainer (2019). TxDb.Hsapiens.UCSC.hg38.knownGene: Annotation package for TxDb object(s). Bioconductor. https://doi.org/10.18129/B9.bioc.TxDb. Hsapiens.UCSC.hg38.knownGene.

- Soneson, C., Love, M.I., and Robinson, M.D. (2015). Differential analyses for RNA-seq: transcript-level estimates improve gene-level inferences. F1000Res. 4, 1521. https://doi.org/10.12688/f1000research.7563.2.
- Robinson, M.D., McCarthy, D.J., and Smyth, G.K. (2010). edgeR: a Bioconductor package for differential expression analysis of digital gene expression data. Bioinformatics 26, 139–140. https://doi.org/10. 1093/bioinformatics/bto616.
- Rainer, J. (2017). EnsDb.Hsapiens.v86: Ensembl based annotation package. Bioconductor. https://doi.org/10.18129/B9.bioc.EnsDb.Hsapiens.v86.
- 87. Wickham, H., Navarro, D., and Pedersen, T.L. (2016). ggplot2: Elegant Graphics for Data. Analysis, [Third Edition] (Springer).
- Bray, N.L., Pimentel, H., Melsted, P., and Pachter, L. (2016). Nearoptimal probabilistic RNA-seq quantification. Nat. Biotechnol. 34, 525–527. https://doi.org/10.1038/nbt.3519.
- Schütze, T.M., Bölicke, N., Sameith, K., and Albert, M. (2023). Profiling Cell Type-Specific Gene Regulatory Regions in Human Cortical Organoids. In Brain Organoid Research, J. Gopalakrishnan, ed. (Springer), pp. 17–41. https://doi.org/10.1007/978-1-0716-2720-4_2.
- Schindelin, J., Arganda-Carreras, I., Frise, E., Kaynig, V., Longair, M., Pietzsch, T., Preibisch, S., Rueden, C., Saalfeld, S., Schmid, B., et al. (2012). Fiji: an open-source platform for biological-image analysis. Nat. Methods 9, 676–682. https://doi.org/10.1038/nmeth.2019.
- Schmidt, U., Weigert, M., Broaddus, C., and Myers, G. (2018). Cell Detection with Star-Convex Polygons. Held in Cham (Springer International Publishing), pp. 265–273.
- Sakib, M.S., Sokpor, G., Nguyen, H.P., Fischer, A., and Tuoc, T. (2021). Intranuclear immunostaining-based FACS protocol from embryonic cortical tissue. STAR Protoc. 2, 100318. https://doi.org/10.1016/j.xpro. 2021.100318.
- Ewels, P.A., Peltzer, A., Fillinger, S., Patel, H., Alneberg, J., Wilm, A., Garcia, M.U., Di Tommaso, P., and Nahnsen, S. (2020). The nf-core framework for community-curated bioinformatics pipelines. Nat. Biotechnol. 38, 276–278. https://doi.org/10.1038/s41587-020-0439-x.
- 94. Amemiya, H.M., Kundaje, A., and Boyle, A.P. (2019). The ENCODE Blacklist: Identification of Problematic Regions of the Genome. Sci. Rep. 9, 9354. https://doi.org/10.1038/s41598-019-45839-z.
- Ramírez, F., Ryan, D.P., Grüning, B., Bhardwaj, V., Kilpert, F., Richter, A. S., Heyne, S., Dündar, F., and Manke, T. (2016). deepTools2: a next generation web server for deep-sequencing data analysis. Nucleic Acids Res. 44, W160–W165. https://doi.org/10.1093/nar/gkw257.
- Picelli, S., Björklund, Å.K., Faridani, O.R., Sagasser, S., Winberg, G., and Sandberg, R. (2013). Smart-seq2 for sensitive full-length transcriptome profiling in single cells. Nat. Methods 10, 1096–1098. https://doi.org/ 10.1038/nmeth.2639.
- Hoffmann, J., Schütze, T.M., Kolodziejczyk, A., Kränkel, A., Reinhardt, S., Derihaci, R.P., Birdir, C., Wimberger, P., Koseki, H., and Albert, M. (2024). Canonical and non-canonical PRC1 differentially contribute to the regulation of neural stem cell fate. Preprint at bioRxiv. https://doi. org/10.1101/2024.08.07.606990.
- Ashburner, M., Ball, C.A., Blake, J.A., Botstein, D., Butler, H., Cherry, J. M., Davis, A.P., Dolinski, K., Dwight, S.S., Eppig, J.T., et al. (2000). Gene ontology: tool for the unification of biology. The Gene Ontology Consortium. Nat. Genet. 25, 25–29. https://doi.org/10.1038/75556.
- 99. Thomas, P.D., Ebert, D., Muruganujan, A., Mushayahama, T., Albou, L.P., and Mi, H. (2022). PANTHER: Making genome-scale phylogenetics accessible to all. Protein Sci. 31, 8–22. https://doi.org/10.1002/pro.4218.
- Schmitz, S.U., Albert, M., Malatesta, M., Morey, L., Johansen, J.V., Bak, M., Tommerup, N., Abarrategui, I., and Helin, K. (2011). Jarid1b targets genes regulating development and is involved in neural differentiation. EMBO J. 30, 4586–4600. https://doi.org/10.1038/emboj.2011.383.



STAR*METHODS

KEY RESOURCES TABLE

REAGENT or RESOURCE	SOURCE	IDENTIFIER
Antibodies		
Goat anti-Sox2	R&D Systems	Cat # AF2018; RRID: AB_355110
Rat anti-Ki67	Invitrogen	Cat # 14-5698-82; RRID: AB_10854564
Rat anti-PH3	Abcam	Cat # ab10543; RRID: AB_2295065
Rat anti-Ctip2 (Clone: 25B6)	Abcam	Cat # ab18465; RRID: AB_2064130
Rabbit anti-Tbr2	Abcam	Cat # ab23345; RRID: AB_778267
Rabbit anti-H3K27me3	Cell Signaling	Cat # 9733; RRID: AB_2616029
Rabbit anti-H3K4me2/3	Cell Signaling	Cat # 9751; RRID: AB_2616028
Rabbit anti-Ezh2 (Clone: D2C9)	Cell Signaling	Cat # 5246; RRID: AB_10694683
Rabbit anti-Suz12	Cell Signaling	Cat # 3737; RRID: AB_2196850
Mouse anti-Zo1, Alexa Fluor™ 647 conjugated	Invitrogen	Cat # MA3-39100-A647; RRID: AB_2663167
Rat anti-Tbr2, PE conjugated	Invitrogen/EBiosciences	Cat # 12-4875-82; RRID: AB_1603275
Rabbit anti-Pax6	BioLegend	Cat # 901301; RRID: AB_2565003
Rabbit anti-CC3	Cell Signaling	Cat # 9661S; RRID: AB_2341188
Rabbit anti-CD138 (Syndecan 1)	Invitrogen	Cat # 36-2900; RRID: AB_2533248
Rat anti-CD29 (active Integrin β1)	BD Biosciences	Cat # 550531; RRID: AB_393729
Mouse anti-Integrin β1 (Clone: P5D2)	Abcam	Cat # ab24693; RRID: AB_448230
Rabbit anti-Laminin (LAMA1)	Sigma Aldrich	Cat # L9393; RRID: AB_477163
Rabbit anti-UTX (KDM6A)	Cell Signaling	Cat # 33510S; RRID: AB_2721244
Oonkey anti-Goat IgG, Alexa Fluor 555 conjugated	Invitrogen	Cat # A-21432; RRID: AB_2535853
Donkey anti-Goat IgG, Alexa Fluor 488 conjugated	Invitrogen	Cat # A11055; RRID: AB_2534102
Donkey anti-Rat IgG, Alexa Fluor 647 conjugated	Invitrogen	Cat # A78947; RRID: AB_2910635
Donkey anti-Rat IgG, Alexa Fluor 555 conjugated	Invitrogen	Cat # A48270; RRID: AB_2896336
Donkey anti-Rat IgG, Alexa Fluor 488 conjugated	Invitrogen	Cat # A21208; RRID: AB_2535794
Donkey anti-Rabbit IgG, Alexa Fluor 555 conjugated	Invitrogen	Cat # A31572; RRID: AB_162543
Donkey anti-Rabbit IgG, Alexa Fluor 488 conjugated	Invitrogen	Cat # A21206; RRID: AB_2535792
Mouse anti-Human Pax6, Alexa Fluor 647 conjugated	BD Pharmingen	Cat # 562249; RRID: AB_11152956
Nouse anti-Tbr2, PE conjugated	BD Pharmingen	Cat # 566749; RRID: AB_2869847
Rat anti-Ctip2, FITC conjugated	Abcam	Cat # ab123449; RRID: AB_10973033
Goat F(ab) anti-Mouse IgG H&L	Abcam	Cat # ab6668; RRID: AB_955960
Goat F(ab) anti-Rat IgG H&L	Abcam	Cat # ab7172; RRID: AB 955962
Guinea Pig anti-Rabbit IgG	Antibodies-Online	Cat # ABIN101961; RRID: AB_10775589
Mouse anti-H3K36me2 (Clone: MABI 0332)	Active Motif	Cat # 61019; RRID: AB_2650523
Rabbit anti-H3ac (pan-acetyl)	Active Motif	Cat # 39139; RRID: AB_2687871
Rabbit anti-H3.3 (Clone: EPR17899)	Abcam	Cat # ab208690
Nouse anti-H3K9me1 (Clone: 7E7.H12)	BioLegend	Cat # 824201; RRID: AB_2564878
Rabbit anti-H3 (Clone: D1H2)	IonPath	Cat # 711501
Nouse anti-H4K5ac (Clone: MABI 0405)	Active Motif	Cat # 61523; RRID: AB 2793668
Rabbit anti-H3K36me3 (Clone: D5A7)	Cell Signaling	Cat # 4909S; RRID: AB_1950414
Rabbit anti-H3K64ac (Clone: EPR20713)	Abcam	Cat # ab251549
Mouse anti-GFAP-143Nd (Clone: G-A-5)	Standard BioTools	Cat # 3143022B; RRID: AB_2938640
Rabbit anti-H4K16ac (Clone: E2B8W)	Cell Signaling	Cat # 13534; RRID: AB_2687581
Rabbit anti-H2A.Z (Clone: EPR6171)	Abcam	Cat # ab150402; RRID: AB_2891240
Mouse anti-H4K20me3 (Clone: 6F8-D9)	BioLegend	Cat # 827701; RRID: AB_2564914
(2.2	9	(Continued on payt or





Continued		
REAGENT or RESOURCE	SOURCE	IDENTIFIER
Mouse anti-human SOX2-150Nd (Clone: O30-678)	Standard BioTools	Cat # 3150019B; RRID: AB_3086680
Mouse anti-H3K27me1 (Clone: MABI 0321)	Active Motif	Cat # 61015; RRID: AB_2715573
Mouse anti-H4K20me1 (Clone: 5E10-D8)	Active Motif	Cat # 39727; RRID: AB_2615074
Rabbit anti-H2AK119ub1(Clone: D27C4)	Cell Signaling	Cat # 8240S; RRID: AB_10891618
Rabbit anti-H3K4me1 (Clone: D1A9)	Cell Signaling	Cat # 5326S; RRID: AB_10695148
Rabbit anti-HOPX	Novus Biologicals	Cat # NBP2-82093; RRID: AB_3423623
Mouse anti-H3K9me2 (Clone: 5E5-G5)	BioLegend	Cat # 815504; RRID: AB_2820126
Mouse anti-SATB1 + SATB2 (Clone: SATBA4B10)	Abcam	Cat # ab51502; RRID: AB 882455
Mouse anti-H3K27me3 (Clone: MABI 0323)	Active Motif	Cat # 61017; RRID: AB_2614987
Rabbit anti-H3K27ac (Clone: D5E4)	Cell Signaling	Cat # 8173S; RRID: AB_10949503
Mouse anti-H4K20me2 (Clone: MABI 0422)	Active Motif	Cat # 61533; RRID: AB_2650525
Mouse anti-Ki67-162Dy (Clone: B56)	Standard BioTools	Cat # 3162012B; RRID: AB_2888928
Rabbit anti-H3R2me2a	Epigentek	Cat # A-3714-100; RRID: AB_2313773
Rat anti-H3K9ac (Clone: 2G1F9)	Active Motif	Cat # A-3714-100, Anib. AB_2313773 Cat # 61663; RRID: AB_2793725
Rabbit anti-p300 (Clone: EPR23753-55)	Abcam	Cat # 61663, NAID. AB_2793725 Cat # ab283721
Rabbit anti-HuD + HuC (Clone: EPR19098)	Abcam	Cat # ab233721
Rabbit anti-Hub + Hub (Clone: EPR 19098)	Abcam	Cat # ab252416 Cat # ab251493
Mouse anti-S110B (Clone: 15F4NB)	Novus Biologicals	Cat # 13060; PRID: AB 2708355
Rabbit anti-H3K9me3 (Clone: D4W1U)	Cell Signaling	Cat # 13969; RRID: AB_2798355
Mouse anti-H3S10ph (Clone: MABI 0312)	Active Motif	Cat # 39636; RRID: AB_2793285
Rabbit anti-TBR2 (Clone: EPR21950-241)	Abcam	Cat # ab261913; RRID: AB_2943175
Mouse anti-H3K4me2 (Clone: MABI 0303)	Active Motif	Cat # 39679; RRID: AB_2793302
Mouse anti-H2A.X (Clone: JBW301)	Merck Millipore	Cat # 05-636; RRID: AB_309864
Mouse anti-Pax6 (Clone: PAX6/498)	Novus Biologicals	Cat # NBP2-34705; RRID: AB_3291566
Mouse anti-H3K27me2 (Clone: MABI 0324)	Active Motif	Cat # 61435; RRID: AB_2793635
Mouse anti-H4 (Clone: mAbcam 31830)	Abcam	Cat # ab238663
Biological samples		
GW12-14 human fetal brain tissue	This study	N/A
Mouse: C57BL/6J	Charles River Laboratories	RRID: IMSR; JAX:000664
Chemicals, peptides, and recombinant proteins		
Matrigel hESC-Qualified Matrix, LDEV-free	Corning	Cat # 354277
Matrigel Growth Factor Reduced (GFR) Basement Membrane Matrix, LDEV-free	Corning	Cat # 354230
EED226	MedChemExpress	Cat # HY-101117
Dimethyl Sulfoxide (DMSO)	Sigma Aldrich	Cat. # D2650-100ML
Recombinant Human Syndecan-1 Protein, CF	R&D Systems	Cat # 2780-SD
Recombinant Human Syndecan-2/ CD362 Protein, CF	R&D Systems	Cat # 2965-SD
Benzonase	Sigma Aldrich	Cat # E1014-25KU
mTeSR1 Complete Kit	Stem Cell Technologies	Cat # 85850
ΓrypLE™ Express Enzyme (1X), no phenol red	Gibco	Cat # 12604021
ReLeSR™	Stem Cell Technologies	Cat # 05873
	Cibas	Cat # 17104019
Collagenase type IV	Gibco	
Collagenase type IV Fris-HCI (pH7.4)	Sigma Aldrich	Cat # T2194
		Cat # T2194 Cat # AM9759
Fris-HCI (pH7.4)	Sigma Aldrich	
Fris-HCl (pH7.4) Sodium chloride	Sigma Aldrich Invitrogen	Cat # AM9759



Continued		
REAGENT or RESOURCE	SOURCE	IDENTIFIER
Digitonin, High Purity	Merck	Cat # 300410-1GM
UltraPure™ BSA (50 mg/mL)	Invitrogen	Cat # AM2618
cOmplete™, Mini, EDTA-free Protease Inhibitor Cocktail	Roche	Cat # 11836170001
RNasin Ribonuclease Inhibitor	Promega	Cat # N261B
BioMag Plus Concanavalin A	Polysciences Inc.	Cat # 86057-3
AMPure XP Reagent	Beckman Coulter	Cat # A63880
Superscript III Reverse Transcriptase	Invitrogen	Cat # 18080044
ightCycler 480 SYBR Green I Master	Roche	Cat # 4887352001
BSA (lyophilized powder)	Sigma Aldrich	Cat # A3858-50g
Spermidine	Sigma Aldrich	Cat # S0266
Calcium chloride	Fisher Scientific	Cat # BP510
Potassium chloride	Sigma Aldrich	Cat # P3911
Manganese chloride	Sigma Aldrich	Cat # 203734
Ethylenediaminetetraacetic acid (EDTA)	Sigma Aldrich	Cat # 03690-100ML
pA-Tn5 Transposase - loaded	Diagenode	Cat # C01070001
TAPS	Sigma Aldrich	Cat # T5130
Friton X-100	Sigma Aldrich	Cat # T9284-500ML
NEBNext High-Fidelity 2X PCR Master Mix	New England Biolabs	Cat # M0541S
Superscript II Reverse Transcriptase	Invitrogen	Cat # 18064022
(APA HiFi HotStart ReadyMix	Roche	Cat # 07958927001
DMEM/F12, HEPES	Gibco	Cat # 31330095
Neurobasal medium	Gibco	Cat # 21103049
3-27™ Supplement (50x), serum-free	Gibco	Cat # 17504044
N-2 Supplement (100X)	Gibco	Cat # 17502048
MEM Non-Essential Amino Acids Solution (100X)	Gibco	Cat # 11140050
GlutaMAX™ Supplement	Gibco	Cat # 35050038
Amphotericin B (Fungizone)	Gibco	Cat # 11520496
KnockOut™ Serum Replacement	Gibco	Cat # 10828010
Dorsomorphine	Stem Cell Technologies	Cat # 72102
\83-01	Stem Cell Technologies	Cat # 72022
CHIR-99021	Stem Cell Technologies	Cat # 72052
SB-431542	Stem Cell Technologies	Cat # 72232
nsulin Solution, Human recombinant	Sigma Aldrich	Cat # 19278
Recombinant Human/Murine/Rat BDNF	PeproTech	Cat # 450-02
Recombinant Human GDNF	PeproTech	Cat # 450-10
Ascorbic acid	Sigma Aldrich	Cat # 1043003
Dibutyryl-cAMP	Stem Cell Technologies	Cat # 73882
Glutamine (200 mM stock)	Gibco	Cat # 25030024
HEPES-NaOH (1M stock)	in-house media kitchen	N/A
Rat serum	Charles River Laboratories	Crl:CD(SD)
JltraPure™ low melting point agarose	Invitrogen	Cat # 16520100
Antibody Stabilizer TRIS	CANDOR Bioscience	Cat # 130050
Cell-ID™ Cisplatin	Standard BioTools	Cat # 201064
Maxpar® X8 Multimetal Labeling Kit – 40 Rxn	Standard BioTools	Cat # 201300
Maxpar MCP9 Antibody Labeling Kit, 111Cd-4	Standard BioTools	Cat # 201111A
Maxpar MCP9 Antibody Labeling Kit, 112Cd-4	Standard BioTools	Cat # 201112A
Maxpar MCP9 Antibody Labeling Kit, 114Cd-4	Standard BioTools	Cat # 201114A
Maxpar MCP9 Antibody Labeling Kit, 116Cd-4	Standard BioTools	Cat # 201116A





Continued		
REAGENT or RESOURCE	SOURCE	IDENTIFIER
Maxpar Cell Staining Buffer	Standard BioTools	Cat # 201068
DPBS	Corning	Cat # 21-031-CV
16 % Formaldehyde (w/v), methanol-free	Thermo Scientific	Cat # 28906
Fetal Bovine Serum (FBS)	Sigma Aldrich	Cat # F7524
Maxpar Nuclear Antigen Staining Buffer Set	Standard BioTools	Cat # 201063
Maxpar Fix I Buffer	Standard BioTools	Cat # 201065
Maxpar 10X Barcode Perm Buffer	Standard BioTools	Cat # 201057
Cell-ID™ Intercalator-Iridium	Standard BioTools	Cat # 201192A
Maxpar Water	Standard BioTools	Cat # 201069
Maxpar Cell Acquisition Solution Plus for CyTOF XT	Standard BioTools	Cat # 201244
EQ™ Six Element Calibration Beads	Standard BioTools	Cat # 201245
Critical commercial assays		
MACS Neural Tissue Dissociation Kit P	Miltenyi Biotec Inc.	Cat # 130-092-628
RNeasy Mini Kit	QIAGEN	Cat # 74104
Neural Tissue Dissociation Kit (P)	Miltenyi Biotec Inc.	Cat # 130-092-628
Cell-ID 20-Plex Pd Barcoding Kit	Standard BioTools	Cat # 201060
Deposited data	Staridard Dio 100io	Gat ii 201000
·	Florio et al. ³⁵	NCBI GEO: GSE65000
RNA-seq		
CUT&Tag Human tissue GW12-14	This paper	Zenodo: https://doi.org/10.5281/ zenodo.13897222
CUT&Tag PRC2 inhibitor treated organoids W8	This paper	Zenodo: https://doi.org/10.5281/ zenodo.13897222
Bulk RNA-seq PRC2 inhibitor treated organoids W8	This paper	Zenodo: https://doi.org/10.5281/ zenodo.13897222
Epi-CyTOF	This paper	FlowRepository: FR-FCM-Z8DC
Experimental models: Cell lines	• •	
Human: CRTDi004-A iPSC	Völkner et al. ⁷⁸	CRTDi004-A; RRID: CVCL_YR23
Human: HPSI0114i-kolf_2 iPSC	Welcome Trust Sanger Institute, HipSci	WTSIi018-B; RRID: CVCL_AE29
Oligonucleotides	cango meman, mpes	
Primers, see Table S7	This paper	N/A
Software and algorithms	ττιο ραρεί	14/7
Fiji/ImageJ	Fiji/ImageJ	https://imagej.nih.gov/ij/
riji/imageJ Prism (8.4.3)	GraphPad software	nttps://imagej.nin.gov/ij/ N/A
	Serif Ltd.	N/A
Affinity Photo + Designer (1.10.5.1342)		
FACSCharre	BD Biosciences	N/A
FACSChorus	BD Biosciences	N/A
CyTOF Software (v9.0.2)	Standard BioTools	N/A
OMIQ	Dotmatics	N/A
FastQC (v0.11.9)	Babraham Bioinformatics	https://www.bioinformatics.babraham. ac.uk/projects/fastqc/
nf-core/cutandrun (v3.2.2)	Cheshire et al. ⁷⁹	N/A
Diffbind (v3.12.0)	Stark et al.80	N/A
DESeq2 (v1.42.1)	Love et al. ⁸¹	N/A
deeptools (v3.5.1)	Yu et al. ⁸²	N/A
ChIPseeker (v1.38.0)	Yu et al. 82 and Bioconductor Core Team and Bioconductor Package Maintainer 83	N/A
ReactomePA (v1.46.0)	Yu et al. 44 and Moore et al. 45	N/A





Continued		
REAGENT or RESOURCE	SOURCE	IDENTIFIER
TxDb.Hsapiens.UCSC.hg38.knownGene (v3.18.0)	Bioconductor Core Team and Bioconductor Package Maintainer ⁸³	N/A
Tximport (v1.30.0)	Soneson et al.84	N/A
edgeR (4.0.16)	Robinson et al. ⁸⁵	N/A
EnsDb.Hsapiens.v86 (v2.99.0)	Rainer et al.86	N/A
Ggplot2 (v3.1.3.1)	Wickham et al.87	N/A
Kallisto (v0.46.1)	Bray et al.88	N/A
Other		
Costar® 6-well Clear Flat Bottom Ultra-Low Attachment Multiple Well Plates	Corning	Cat # 3471
DNA LoBind microcentrifuge tubes, 1.5 mL	Eppendorf	Cat # 0030108051
Fisherbrand™ RNase-Free Disposable Pellet Pestles	Fisher Scientific	Cat # 12-141-368
Filcon Sterile 70μm Cup Strainer	BD Biosciences	Cat # 340633
Ultrafree-MC, VV 0,1 μm Centrifgual Filters	Merck	Cat # UFC30VV00
Falcon® 5 mL Round Bottom Polystyrene Test Tube, with Cell Strainer Snap Cap	Corning	Cat # 352235

EXPERIMENTAL MODEL AND SUBJECT DETAILS

Human fetal tissue

Human fetal brain tissue was obtained from the Department of Gynecology and Obstetrics, University Clinic Carl Gustav Carus of the Technische Universität Dresden, following elective pregnancy termination and informed written maternal consents, and with approval of the local University Hospital Ethical Review Committee (IRB00001473; IORG0001076; ethical approval number EK 355092018), in accordance with the Declaration of Helsinki. The age of fetuses ranged from gestation week (GW) 12 to 14, as assessed by ultrasound measurements of crown-rump length and other standard criteria of developmental stage determination. These developmental time points correspond to an early/mid-neurogenic stage, when the outer SVZ expands, and the production of upperlayer neurons starts. Due to the protection of data privacy, the sex of the human fetuses, from which the human neocortex tissue was obtained, cannot be reported. The sex of the human fetuses is not likely to be of relevance to the results obtained in the present study. The fetal human neocortex tissue samples used in this study reported no health disorders. Fetal human brain tissue was dissected in Tyrode's solution and used immediately for fixation, processed for CyTOF or snap-frozen for CUT&Tag.

Human induced pluripotent stem cell lines

All experiments involving hiPSCs were performed in accordance with the ethical standards of the institutional and/or national research committee, as well as with the 1964 Helsinki Declaration, and approved by the University Hospital Ethical Review Committee (IRB00001473; IORG0001076; ethical approval number SR-EK-456092021). Human cortical organoids were generated using the previously generated male human iPSC lines CRTDi004-A⁷⁸ and HPSI0114i-kolf_2 (Welcome Trust Sanger Institute, HipSci), derived from healthy donors. The human iPSC lines were maintained on Matrigel-coated (Corning, 354277) culture dishes in mTeSR1 (Stem Cell Technologies, 85850) and passaged using TrypLE Express enzyme (Gibco, 12604021) (CRTDi004-A) or ReLeSR (HPSI0114i-kolf_2) (Stem Cell Technologies, 05873).⁸⁹

Mice

All experimental procedures were conducted in agreement with the German Animal Welfare Legislation after approval by the Landesdirektion Sachsen (licenses 25-5131/603/9). Animals were kept on a 12-h/12-h light/dark cycle with food and water ad libitum. All mice were wildtype mice from the inbred C57BL/6J strain. Embryonic day (E) 0.5 was set as noon on the day on which the vaginal plug was observed. All experiments were performed in the dorsolateral telencephalon of mouse embryos. The sex of embryos was not determined, as it is not likely to be relevant to the results obtained in the present study.

METHOD DETAILS

Cortical organoid culture

Human cortical organoids were generated following the sliced neocortical organoid (SNO) protocol, previously described in detail. ^{31,52,89} Briefly, hiPSC colonies (ca. 1.5 mm in diameter) were detached using collagenase (Gibco, 17104019) and transferred





to ultra-low attachment six-well plates (Corning, 3471), containing forebrain medium 1, to form embryoid bodies (EBs). EBs were embedded in Matrigel (Corning, 354230) with 20-25 EBs per Matrigel cookie on day 7. The following week (days 7-14), EBs were maintained in forebrain medium 2, with media changes every other day. On day 14, the organoids were released from the Matrigel. Culture is continued in six-well ultra-low attachment plates in forebrain medium 3 on an orbital shaker at 100 rpm. From day 35, forebrain medium 3 is supplemented with 1% v/v Matrigel. On day 45, organoids were cut on a vibratome into 500-µm-thick slices, to increase supply of oxygen and nutrients throughout the organoids. Therefore, organoids were embedded in 3% low melting point agarose. Slicing of organoids was repeated at 10 weeks. From day 72, organoids were maintained in forebrain medium 4.

For PRC2 inhibitor treatment, 10 mM EED226 stock solution (MedChemExpress, HY-101117) 41 was added to the culture medium to a final concentration of 0.25 μ M, 0.5 μ M or 5 μ M. For the control condition, an equal volume of DMSO (Sigma Aldrich, D2650-100ML) was added, corresponding to 0.05% DMSO. EEDi treatment was only compared to the DMSO condition for all analyses, as we noted that DMSO had some effects on H3K27me3 levels (but not on PH3, proportion of cell types or organoid size). Medium supplemented with EED226 or DMSO was prepared fresh for each media change. Treatment was started on day 21 of organoid culture and continued until day 56.

For treatment with ECM proteins, organoid medium was supplied with a final concentration of 500 ng/ml Syndecan 1 (R&D Systems, 2780-SD) or Syndecan 2 (R&D Systems, 2965-SD), and an equal volume of PBS was added for the control condition, corresponding to 0.1% PBS. Organoid medium with ECM proteins was prepared fresh for each media change. Treatment was started on day 21 of organoid culture and continued until day 35.

Mouse hemisphere rotation culture

Mouse brain hemisphere rotation culture (HERO) was performed as previously described. 52 E14.5 brains were dissected in cold PBS. Before separating the hemispheres, the meninges was removed. Hemispheres were then transferred into a rotating flask with 1.5 mL of Neurobasal medium supplemented with 10% rat serum, 20 μ M glutamine, 1X penicillin/streptomycin, 1X N-2 and 1X B-27 supplement and 0.1 M HEPES-NaOH, pH 7.2. HERO culture was performed for 24 h in a Whole Embryo Culture System (Nakayama, 10-0310) in a humidified atmosphere of 40% O_2 , 5% CO_2 and 55% N_2 at 37°C. For treatment of the hemispheres, 500 μ g/ml Syndecan 1 and Syndecan 2 stock solution was added to the culture medium to a final concentration of 500 ng/ml or 5 μ g/ml. For the control condition, an equal volume of PBS was added, corresponding to 5% PBS. Additionally, for PRC2 inhibitor treatment, 10 mM EED226 stock solution was added to the culture medium to a final concentration of 5 μ M. For the control condition, an equal volume of DMSO was added, corresponding to 0.05% DMSO. Integrin blocking was carried out using an antibody against Integrin β 1 (Abcam, ab24693) at a 1:100 dilution.

Metal isotope conjugation of antibodies

The antibodies used for the Epi-CyTOF staining were either purchased conjugated with a defined metal isotope or purified within a BSA-free buffer (Table S1). Among those antibodies many were previously validated. The conjugation of 100 μ g purified antibody with a defined heavy metal tag was done with the MaxPar Antibody Conjugation Kit (Standard BioTools) according to the manufacturer's recommendations. The protein concentration of the labelled antibodies was measured with a spectrophotometer (Nanodrop 2000c, Thermo Scientific) and adjusted to 0.5 mg/ml with an antibody stabilizer solution (Candor Bioscience, 130050).

Tissue dissociation for Epi-CyTOF

To prepare the single cell suspensions for the Epi-CyTOF staining, 8-10 cortical organoids (W8) or rice grain sized pieces of human fetal tissue were dissociated using the MACS Neural Tissue Dissociation Kit P (Miltenyi Biotec Inc., 130-092-628) with an incubation time of 6 min for organoids and 15 min for fetal tissue for enzyme mix 1. Subsequently, the cell pellets were resuspended in 500 μl cold DPBS (Corning, 21-031-CV) and incubated for 10 min with 1 μl Benzonase (1:500, Sigma, E1014-25KU) to prevent cell clumping and 0.625 μl cisplatin (1:800, Cell-ID[™], ¹⁹⁵Pt, Standard BioTools, 201064) for cell viability staining. From this step onwards, all centrifugation steps were carried out at room temperature (RT). Subsequently, the samples were centrifuged for 7 min at 300 x g and washed with 2 ml Maxpar cell staining buffer (CSB; Standard BioTools, 201068) followed by fixation with 1.6% paraformaldehyde (PFA, methanol-free, diluted in DPBS; Thermo Scientific, 28906) for 10 min at RT on a rotator. The samples were centrifuged at 900 x g for 10 min and washed twice with 2 ml CSB. Finally, the cell pellets were resuspended in freezing medium (20% fetal bovine serum (FBS, Sigma, F7524), 10 % dimethyl sulfoxide (DMSO, Sigma, D8418-100ML) in DMEM) and aliquoted (1-2 Mio. cells/ml) before storage store at -70°C.

Palladium-based barcoding and cell staining for Epi-CyTOF

For barcoding and staining, the frozen samples were immediately thawed in a water bath at 37°C and washed with 2 ml CSB. All centrifugation steps are performed at RT. After centrifugation at 900 x g for 10 min, the pellets were resuspended in Maxpar Nuclear Antigen Staining buffer working solution (Mixed 1 part concentrated, 3 parts diluted, Standard BioTools, 201063) and incubated for 30 min at RT for permeabilization. Afterwards, the cells were washed twice by 2 ml Maxpar Nuclear Antigen Staining Perm (NP) buffer (Standard BioTools, 201063), with centrifugations at 900 x g for 10 min. Next, the cell pellets were resuspended in 1X Fix I Buffer (Standard BioTools, 201065) diluted in PBS and incubated for 10 min at RT, followed by a centrifugation at 900 x g for 10 min. The cells were washed twice with 1 ml 1X Barcode Perm Buffer (Standard BioTools, 201057). After centrifugation at 900 x g for



10 min, each sample was resuspended in 200 µl 1X Barcode Perm Buffer. For multiplexing by barcoding, 2.5 µl Palladium barcodes (Cell-ID™ 20-Plex Pd Barcoding Kit, Standard BioTools, 201060) were mixed with 25 µl Barcode Perm buffer, added to each sample separately, and incubated for 30 min at RT. Afterwards, the samples were washed with 2 ml Maxpar CSB and centrifugated at 900 x g for 10 min. The cell pellets were resuspended in 100 µl CSB and pooled in one tube. Up to three million cells were blocked in 50 µl 1% BSA diluted in NP buffer for 10 min at RT before adding 50 µl pre-mixed and filtered (Merck, UFC30VV00) antibody master mixture in NP. After 1 h of staining at RT, the cells were washed with 2 ml CSB, pelleted at 900 x g for 10 min and resuspended in 1 ml Cell-ID™ Intercalator-Iridium (Standard BioTools, 201192A, 1:1000 in Maxpar Fix Perm Buffer). Additional 125 µl 16% PFA (methanol-free, 28906, Thermo Scientific) were added, and the samples were fixed for 30 min at RT. Finally, the cells were washed with 2 ml CSB, pelleted at 900 x g for 10 min and resuspended in 1 ml freezing medium (20% FBS and 10 % DMSO in DMEM) to preserve samples at -70°C until measurement.

CyTOF measurement

The stained and frozen multiplexed sample pools were washed with 2 ml Maxpar cell staining buffer (CSB, Standard BioTools, 201068) and centrifugated at 900 x g for 10 min. The cell pellet was washed with 2 ml Maxpar water (Standard BioTools, 201069), filtered through a 35 μm cell strainer (Falcon, 352235) and counted with the MACSQuant Analyzer (Miltenyi Biotec). For cell acquisition, the cell concentration was adjusted to 6 x 10⁵ cells per ml with Maxpar cell acquisition solution plus (CASplus, Standard BioTools, 201244). An instrument calibration and tuning were performed using EQ six element calibration beads (Standard BioTools, 201245) before sample analysis. The calibration beads contain a defined concentration of the metal isotopes 89Y, 115In, 140Ce, 159Tb, ¹⁷⁵Lu and ²⁰⁹Bi, and were added 10% v/v as internal standard to each sample solution for detector voltage optimization during measurements. The samples were acquired with the suspension mass cytometer CyTOF2 and CyTOF XT (Standard BioTools) with a constant flow rate of 30 µl and approximately 200 events per second. The recorded raw and linear mode data (LMD) files contain time-of-flight (TOF, m/z) spectra and digitalized ion signals for every 13 µs push from all available mass channels. For single-cell event detection, the CyTOF software (v9.0.2) was used to convolute and smoothen the total current and pulse intensity to generate an event length parameter. The created FCS 3.1 contains randomized and normalized data for downstream analysis. The debarcoder function within the CvTOF software was used to generate separate FCS files per sample from the multiplexed pool file based on the individual 6-choose-3 Pd scheme that was used for barcode staining. The intensities of the six Pd isotopes were utilized to define optimal parameter settings for a minimal barcode separation (BcS) and a maximal mahalanobis distance (MD) to distinguish desired events.

Epi-CyTOF data analysis

Data clean-up and analysis was performed on the cloud-based software OMIQ (Dotmatics). FCS files were scaled after hyperbolic arcsine (arcsinh) transformation with a cofactor of 5. Manual gating was used for data cleanup to remove ion clouds, aggregates, and debris based on the event length and the gaussian parameter center, width, offset, and residual. EQ bead signals were removed by 140-cerium isotope (140 Ce) low gating. Cellular events were identified based on the 191/193-iridium (191 Ir and 193 Ir) signal that was also used in combination with event length parameter to remove doublets. Finally, dead cells were excluded by the positive 196-cisplatin (196 Pt) signal to subsample the viable cell population for downstream analysis. Three main neural cell type populations were defined according to the expression of SOX2, PAX6, TBR2, and CTIP2. A standardised gating hierarchy led to three defined cell clusters. First, all TBR2+ events were selected (IPs). Moreover, TBR2- events were further divided into the SOX2+PAX6+/CTIP2- (RG) or CTIP2+/SOX2-PAX6- (neurons) populations. Uniform Manifold Approximation and Projection (UMAP) was used as the dimensionality reduction algorithm to illustrate the global structure of the 12 samples based on the expression of the 10 cell type-specific markers (neighbors= 15, minimum distance= 0,4, metric: Euclidean, epochs= 200, random seed= 815, embedding initialization: spectral). The expression level of the epigenetic markers was illustrated specifically within the clustered data as color-continuous scatter plots. Averages of median metal tag intensities of 4 replicates were calculated and normalized to the highest value across cell populations for each marker separately. These values were transformed into log2(FC) and illustrated in heat maps (Graph Pad/Prism software, version 9).

Immunofluorescence staining

For immunofluorescence (IF) staining, cortical organoids were removed from culture medium, transferred into 4% PFA in 120 mM phosphate buffer pH 7.4 and fixed for 30 min at RT. Human fetal tissue and mouse hemispheres were kept in 4% PFA solution for 24 h at 4°C. After removing the PFA solution, the tissue was washed twice for 5 min with PBS. Human fetal tissue was subsequently transferred to 15% Sucrose in PBS, incubated at 4°C overnight and then transferred to 30% Sucrose in PBS before storage at 4°C. Cortical organoids and mouse hemispheres were directly stored in 30% Sucrose in PBS after fixation and washing. Sucrose-infiltrated tissue was washed in a 1:1 mixture of 30% Sucrose in PBS and OCT before embedding in the same mixture was performed in cryomolds on dry ice.

Subsequently, 20 µm cryosections were prepared and stored at -20°C until staining. IF staining was performed as previously described. Slides containing cryosections were dried for 5 min at RT and briefly washed with PBS before antigen retrieval was performed in 10 mM citrate buffer pH 6.0 for 1 h at 70°C. Following a 5 min PBS wash, the slides were covered with blocking buffer (10% horse serum and 0.1% Triton X-100 in PBS) for 30 min at RT. Afterwards the sections were incubated with the primary antibodies





diluted in blocking buffer overnight at 4° C. The following antibodies were used for staining: Rat anti-Ctip2 (1:250, Abcam ab18465); Rat anti-Ki67 (1:500, Invitrogen 14-5698-82); Goat anti-Sox2 (1:200, R&D Systems AF2018); Rat anti-PH3 (1:500, Abcam ab10543); Rabbit anti-Histone H3K27me3 (1:1600, Cell Signaling 9733); Rabbit anti-Histone H3K4me2/3 (1:500, Cell Signaling 9751); Rabbit anti-Ezh2 (1:200, Cell Signaling 5246); Rabbit anti-Suz12 (1:800, Cell Signaling 3737); Mouse anti-Zo1 (1:750, Invitrogen MA3-39100-A647⁴¹); Rat anti-Tbr2 (1:33, Invitrogen 12-4875-82⁴¹); Rabbit anti-Pax6 (1:300, BioLegend 901301), Rabbit anti-CC3 (1:400, Cell Signaling 9661S); Rabbit anti-CD138 (Syndecan 1, 1:100, Invitrogen 36-2900); Rat anti-CD29 (active Integrin β 1, 1:200, BD Biosciences 550531); Rabbit anti-Laminin (LAMA1, 1:200, Sigma Aldrich L9393), and Rabbit anti-UTX (KDM6A, 1:200, Cell Signaling 33510S). The next day, the slides were washed three times for 5 min with PBS, before addition of the secondary antibodies (1:1000) and DAPI (1:1000) diluted in blocking buffer and incubation for 1-2 h at RT. Finally, the slides were washed three times for 5 min with PBS and mounted with Mowiol before long term storage at 4° C.

Images were acquired using a Zeiss ApoTome2 fluorescence microscope with a 20x objective and 1.5-μm thick optical sections. Images are depicted as maximum intensity projections of 10–15 optical sections. Stitching of acquired tile scans was performed using the ZEN software.

Image analysis

All samples were blinded before the acquisition of the data. Quantification was performed using Fiji, ⁹⁰ processed using Excel (Microsoft), and plotted using Prism (Graphpad Software). Image quantifications were performed either manually or using the Fiji plugin StarDist. ⁹¹ Briefly, images were analyzed as maximum intensity projections and first cropped to separate the different cortical layers (VZ, SVZ, IZ, CP for fetal human tissue and VZ, SVZ/CP for cortical organoids). Subsequently, all channels were split to use the StarDist 2D plugin in the versatile (fluorescent nuclei) model. If necessary, segmentation was corrected manually. Manual quantifications were performed using the cell counter tool or fluorescence intensity measures in Fiji. For cortical organoids, only ventricles facing the outside of the organoid were analyzed, as ventricles in the organoids' center might suffer from reduced oxygen and nutrient supply. ³¹ The borders of microscopy images are indicated by yellow dotted lines, and supplemented with black boxes to display rectangles of equal size for subpanels.

Isolation of neural cell populations for CUT&Tag and RNA-seq

Whole organoids or rice grain sized pieces of human fetal tissue were transferred to cryovials. After liquids were entirely removed, the vials were snap frozen on dry ice and stored at -70°C until further processing. The nuclei isolation procedure was modified from a previously described. ⁹² Using forceps, the frozen tissue was transferred to a microcentrifuge tube and 500 μ l Lysis Buffer (10 mM Tris-HCl pH 7.4, 10 mM NaCl, 3 mM MgCl2, 1% BSA, 0.01% Tween-20, 0.01% NP40 Substitute, 0.001% Digitonin in H2O) were added before homogenizing with a pellet pestle (Fisher Scientific, 12-141-368) 15 times. The homogenized samples were incubated on ice for 2 min and mixed 10 times with a wide bore pipet tip followed by 2 more minutes of incubation on ice. With a regular tip, 500 μ l chilled wash buffer (10 mM Tris-HCl pH7.4, 10 mM NaCl, 3 mM MgCl2, 1% BSA, 0.1% Tween-20 in H2O) were added to each tube and mixed 5 times. The cell suspension was passed through a 70 μ m cell strainer (BD Bioscience, 340633) into a LoBind tube followed by additional 300 μ l wash buffer. The samples were centrifuged at 500 x g for 5 min at 4°C. The supernatant was removed, and pellets were resuspended in 1 ml of nuclei suspension buffer (NSB; 1% BSA, 1X Protease inhibitor EDTA free, 0.1X RNase inhibitor in PBS). The centrifugation and resuspension steps were repeated once before starting the suspension staining.

For staining, the Alexa Fluor 647 Mouse Anti-Human PAX-6 (BD Pharmingen, 562249, 1:40), PE Mouse Anti-EOMES (BD Pharmingen, 566749, 1:200) and FITC Rat Anti-CTIP2 (Abcam, ab123449, 1:500) antibodies were diluted in the nuclei suspension and incubated on a rotator for 1 h at 4° C in the dark. The stained nuclei suspension was centrifuged for 5 min at 500 x g at 4° C. Following centrifugation, the supernatant was removed, and the pellet was resuspended in 1 ml NSB. This wash step was repeated once before resuspending in 2 ml NSB, flowing the sample through a 40 μ m cell strainer and performing FANS using a BD FACSDiscover S8 Cell Sorter.

IPs were isolated as all TBR2⁺ nuclei. Out of the TBR2⁻ population, CTIP2⁺/PAX6⁻ nuclei were sorted as neurons, while RG were isolated as PAX6⁺/CTIP2⁻. For bulk RNA-seq, 10,000 nuclei were sorted per cell type, while 50,000 nuclei per cell type were used for CUT&Tag.

Gene expression analysis by RT-qPCR

Gene expression analysis was performed as previously described. ^{18,52} For RT-qPCR, RNA was isolated from 10,000 nuclei (after FANS) using the RNeasy Mini kit (Qiagen, 74104). cDNA was synthesized using random hexamers and Superscript III Reverse Transcriptase (Invitrogen, 18080044) and qPCR was performed with LightCycler 480 SYBR Green I Master Mix (Roche, 4887352001) on a LightCycler 480 (Roche). For each sample, three technical replicates were run. Gene expression data was normalized based on the housekeeping gene *GAPDH*. Primers are listed in Table S8.

CUT&Tag library preparation

CUT&Tag was performed based on the protocol published previously. ³⁸ The CUT&Tag direct protocol version used was described in detail: https://doi.org/10.17504/protocols.io.bqwvmxe6. Briefly, 50,000 nuclei per cell type (RG, IP and neurons) were sorted into antibody buffer. Prior to starting the CUT&Tag protocol, the nuclei were centrifuged at 500 x g for 5 min at 4°C, supernatant was



removed and the nuclei were resuspended in $50 \,\mu$ l wash buffer and transferred into PCR tubes. Nuclei were subsequently bound to ConA beads (Polysciences Inc., 86057-3) by adding $3.5 \,\mu$ l ConA beads resuspended in binding buffer to each sample and incubating for 10 min on a rotator at RT.

All following wash steps were performed on a magnetic rack. For blocking of the staining antibodies used for FANS, the supernatant was removed, and the bead-bound nuclei were resuspended in antibody buffer containing 1:1000 Goat F(ab) Anti-Mouse IgG H&L (Abcam, ab6668, RRID: AB_955960) and Goat F(ab) Anti-Rat IgG H&L (Abcam, ab7172, RRID: AB_955962). Blocking was performed for 15 min at RT, followed by two wash steps with 100 μ l antibody buffer. The bead-bound nuclei were subsequently resuspended in 25 μ l antibody buffer containing either 1:50 Rabbit Anti-H3K27me3 (Cell Signaling, 9733) or 1:50 Rabbit Anti-Histone H3K4me2/3 (Cell Signaling, 9751). The primary antibody staining was performed for 1 h on a rotator at RT followed by rotation at 4°C overnight. After removing the primary antibody, the beads were suspended in 25 μ l wash buffer containing 1:100 Guinea Pig Anti-Rabbit IgG (Antibodies-Online, ABIN101961). The secondary antibody was incubated for 45 min on a rotator at RT followed by three washes with 200 μ l wash buffer. Pre-loaded pA-Tn5 (Diagenode, C01070001) was diluted 1:250 in 300 buffer and 25 μ l were added per sample. After 1 h of incubation on a rotator at RT, samples were washed three times with 200 μ l 300-buffer. For tagmentation, the beads were resuspended in 50 μ l tagmentation buffer and incubated at 37°C for 1 h. Finally, the bead-bound nuclei were washed with 50 μ l TAPS wash buffer, and resuspended in 5 μ l 0.1% SDS. To release the DNA the samples were incubated at 58°C for 1 h.

Amplification was performed by addition of 15 μ l Triton neutralization solution, 4 μ l primer mix (containing 10 μ M i5 and i7 uniquely barcoded primers, primers are listed in Table S8) and 25 μ l NEBNext High-Fidelity 2X PCR Master Mix (New England Biolabs, M0541S). The following PCR program was run: 5 min 58°C, 5 min 72°C, 30 s 98°C, 13 times [10 s 98°C, 10 s 60°C], 1 min 72°C, hold 8°C. PCR products were subsequently cleaned up using AMPure XP beads (Beckman Coulter, A63880) at a ratio of 1.3. Sequencing was performed after quantification using a Fragment Analyzer (Agilent) on an Illumina Novaseq 6000 with an average sequencing depth of 20 million fragments.

CUT&Tag data analysis

CUT&Tag bioinformatics analysis was done using the Nf-core cutandrun pipeline (v3.2.2), ^{79,93} with "–genome hg38 –macs-gsize 2805665311 –mito_name 'chrM' –normalization_binsize 1 –use_control 'false' –dedup_target_reads –peakcaller SEACR –seacr_peak_threshold 0.01" and default settings otherwise. The blacklist provided was derived from. ⁹⁴ The pipeline automatically runs all required steps on a library-level, including (but not limited to) raw read quality control, adapter trimming, alignment, filtering, generation of coverage tracks, peak calling and peak quality control. Finally, a consensus peak set is created across all libraries ("–consensus_peak_mode all") or libraries from the same cell type ("–consensus_peak_mode group"). H3K27me3 and H3K4me2/3 CUT&Tag data was processed separately. All datasets acquired from human fetal tissue were CPM normalized ("–normalisation_mode CPM"). Data acquired from inhibitor and DMSO treated cortical organoids was used unnormalized ("–normalisation_mode None"), as CPM normalization was not appropriate for portraying the strong differences expected between the two analysed conditions. For direct comparison of the two histone marks, consensus peak sets generated within the Nf-core pipeline were used.

The Nf-core pipeline output for each histone modification was further processed with the R package Diffbind (v 3.12.0)⁸⁰ for visualization and differential analysis. Raw reads and called peaks were imported and counts were generated within previously determined consensus peak regions without centering the summits. Generated counts for human fetal tissue data were normalized by library size while counts for the cortical organoid data were used unnormalized due to the expected differences in library size. Regions of differential enrichment were determined with DESeq2 (v1.42.1)⁸¹ (p-adjust < 0.05; logFC > 1). Heatmaps and profile plots displaying histone mark enrichment were generated using deeptools (v3.5.1).⁹⁵ Regions identified to be enriched for a histone modification were annotated to genomic features and the nearest neighbouring gene using the R packages ChIPseeker (v1.38.0)⁸² and TxDb.Hsapiens.UCSC.hg38.knownGene (v3.18.0).⁸³ Pathway analysis for those identified genes was performed using ReactomePA (v1.46.0) analysis.⁴⁴

RNA-seq library preparation

Transcriptome libraries were prepared using the SmartSeq-2 protocol, ⁹⁶ as previously described. ⁵² Isolated total RNA from an equivalent of 10,000 nuclei was denatured for 3 min at 72°C in 4 μl hypotonic buffer (0.2% Triton X-100) in the presence of 2.5 mM dNTP, 100 nM dT-primer and 4 U RNase Inhibitor (Promega, N2611). Reverse transcription was performed at 42°C for 90 min after filling up to 10 μl with RT buffer mix for a final concentration of 1X Superscript II buffer (Invitrogen, 18064022), 1 M betaine, 5 mM DTT, 6 mM MgCl2, 1 μM TSO-primer (Table S8), 9 U RNase inhibitor, and 90 U Superscript II. The reverse transcriptase was inactivated at 70°C for 15 min. For subsequent PCR amplification of the cDNA the optimal PCR cycle number was determined with an aliquot of 1 μl unpurified cDNA in a 10 μl qPCR containing 1X KAPA HiFi Hotstart Readymix (Roche, 07958927001), 1X SYBR Green, and 0.2 μM UP-primer (Table S8). The residual 9 μl cDNA were subsequently amplified using KAPA HiFi HotStart Readymix (Roche, 07958927001) at a 1X concentration together with 250 nM UP-primer under the following cycling conditions: initial denaturation at 98°C for 3 min, 12 cycles [98°C 20 s, 67°C 15 s, 72°C 6 min] and final elongation at 72°C for 5 min. Amplified cDNA was purified using 1X volume of Sera-Mag SpeedBeads (GE Healthcare) resuspended in a buffer consisting of 10 mM Tris, 20 mM EDTA, 18.5% (w/v) PEG 8000, and 2 M sodium chloride solution. The cDNA quality and concentration were determined using a Fragment Analyzer (Agilent).





For library preparation, 2 µl amplified cDNA was tagmented in 1X Tagmentation Buffer using 0.8 µl bead-linked transposome (Illumina DNA Prep, (M) Tagmentation, Illumina) at 55°C for 15 min in a total volume of 4 μl. The reaction was stopped by adding 1 µl of 0.1% SDS (37°C, 15 min). Magnetic beads were bound to a magnet, the supernatant was removed, beads were resuspended in 14 μl indexing PCR Mix containing 1X KAPA Hifi HotStart ReadyMix (Roche) and 700 nM unique dual indexing primers (i5 and i7), and subjected to a PCR (72°C 3 min, 98°C 30 s, 12 cycles [98°C 10 s, 63°C 20 s, 72°C 1 min], and 72°C 5 min). Libraries were purified with 0.9X volume Sera-Mag SpeedBeads, followed by a double size selection with 0.6X and 0.9X volume of beads. Sequencing was performed after quantification using a Fragment Analyzer on an Illumina Novaseq 6000.

For transcriptomic analysis of whole W5 cortical organoids, mRNA was isolated from on average 100 ng total RNA by poly-dT enrichment using the Watchmaker mRNA Capture Kit according to the manufacturer's instructions. Samples were then directly subjected to the workflow for strand-specific RNA-Seq library preparation (Watchmaker RNA Library Prep Kit). For ligation xGenTM Stubby Adapters from IDT were used. After ligation, adapters were depleted by an XP bead purification (Beckman Coulter) adding the beads solution in a ratio of 0.7:1 to the samples. Unique dual indexing was done during the following PCR enrichment (13 cycles) using uniquely barcoded primer mixes (i5 and i7). After one more XP bead purification (1:1), libraries were quantified using the Fragment Analyzer NGS-Kit 1-6000bp (Agilent). Libraries were sequenced on an Illumina NovaSeq 6000 S4 Flowcell in 100 bp paired-end mode to a depth of 50 million fragments per library.

RNA-seq data analysis

RNA-seq data analysis was performed as previously described. 52,97 Quality control of the sequencing data was performed with FastQC (v0.11.9). Kallisto (v0.64.1)⁸⁸ was used to align reads to human GRChg38. For further processing, the 10-15 million mapped reads were imported into R using Tximport (v1.30.0)84 and EnsDb.Hsapiens.v86 (v2.99.0).86 Raw fragment normalization based on library size and testing for differential expression between cell types and conditions was performed with edgeR package (v4.0.16)85 with a false discovery rate (FDR) of 5% and a Log2 fold change threshold of 0.5. Volcano plots and heatmaps were generated with the R-packages Ggplot2 (v3.1.3.1).87 Differentially expressed genes were analysed by gene ontology (https://geneontology.org/)98,99 analysis.

Statistical analysis

Sample sizes are reported in each figure legend. Sample sizes were estimated based on previous literature. 18,52,100 All statistical analysis was performed using Prism (GraphPad Software). Normal distribution of datasets was tested by Shapiro-Wilk or Kolmogorov-Smirnov test. The tests used are indicated in the figure legend for each quantification. Significant changes are indicated by stars for each graph and described in the figure legends.